

Citation for published version:

Yongqi Xie, Yang Zhou, Dongsheng Wen, Hongwei Wu, George Haritos, and Hongxing Zhang, 'Experimental investigation on transient characteristics of a dual compensation chamber loop heat pipe subjected to acceleration forces', *Applied Thermal Engineering*, Vol. 130: 169-184, February 2018.

DOI:

<https://doi.org/10.1016/j.applthermaleng.2017.11.014>

Document Version:

This is the Accepted Manuscript version.

The version in the University of Hertfordshire Research Archive may differ from the final published version.

Copyright and Reuse:

© 2017 Elsevier Ltd.

This manuscript version is made available under the terms of the Creative Commons Attribution-NonCommercial-NoDerivatives License CC BY NC-ND 4.0

(<http://creativecommons.org/licenses/by-nc-nd/4.0/>), which permits non-commercial re-use, distribution, and reproduction in any medium, provided the original work is properly cited, and is not altered, transformed, or built upon in any way.

Enquiries

If you believe this document infringes copyright, please contact the Research & Scholarly Communications Team at rsc@herts.ac.uk

1 **Experimental investigation on transient characteristics of a dual compensation chamber**
2 **loop heat pipe subjected to acceleration forces**

3
4 **Yongqi Xie^{a,*}, Yang Zhou^a, Dongsheng Wen^b,**
5 **Hongwei Wu^{c,**}, George Haritos^c, Hongxing Zhang^d**

6
7 ^aSchool of Aeronautic Science and Engineering, Beihang University, Beijing, 100191, China

8 ^bSchool of Chemical and Process Engineering, University of Leeds, Leeds, LS2 9JT, United Kingdom

9 ^cSchool of Engineering and Technology, University of Hertfordshire, Hatfield, AL10 9AB, United Kingdom

10 ^dBeijing Key Laboratory of Space Thermal Control Technology, China Academy of Space Technology, Beijing,
11 100094, China

12
13 *Corresponding author: Tel: +86(10) 8233 8081, Fax.: +86(10) 8233 8952, E-mail: xyq@buaa.edu.cn

14 **Corresponding author: Tel.: +44(0)1707 284265, Fax.: +44(0)1707 285086, E-mail: h.wu6@herts.ac.uk

15
16 **Abstract:** In this article, an experimental study has been conducted to provide better
17 understanding of the transient characteristics of a dual compensation chamber loop heat pipe
18 (DCCLHP) subjected to the acceleration force. A new acceleration test rig was set up to
19 provide the acceleration up to 11 g with three different directions. The heat load on the
20 evaporator ranging from 25 W to 300 W was applied with the acceleration force simultaneously.
21 Experimental results indicated that the DCCLHP could start up at a small heat load of 25 W
22 and the startup behavior was different under acceleration direction conditions because of the
23 vapor-liquid distribution change in the evaporator and compensation chambers (CCs). Under
24 the current operating conditions, the effect of acceleration force was significant to the operating
25 performance at small heat loads whereas was weak at large heat loads. Experimental results
26 also clearly showed that both acceleration magnitude and direction can alter the operating
27 mode. What's more, it was found that temperature oscillation, reverse flow and evaporation in
28 the evaporator core phenomena occurred under acceleration conditions.

29
30 **Keywords:** Loop heat pipe; Dual compensation chambers; Startup behavior; Operating
31 characteristics; Acceleration force; Electronic device cooling

34 **Nomenclature**

35	A	Section area, m^2
36	c	Specific heat capacity, $J/(kg \cdot K)$
37	g	Gravitational acceleration, $9.81 m/s^2$
38	G	Thermal conductance, W/k
39	I	Output current, A
40	L	Distance, m
41	m	Mass flow rate, kg/s
42	Q	Heat load, W
43	R	Physical quantity
44	T	Temperature, K
45	U	Output voltage, V
46	ΔT	Temperature difference, K
47	x	Measured variable
48	λ	Thermal conductivity, $W/(m \cdot K)$

49 **Acronyms**

50	CC	Compensation chamber
51	CCM	Constant conductance mode
52	DCCLHP	Dual compensation chamber loop heat pipe
53	LHP	Loop heat pipe
54	RTD	Resistance temperature detector
55	VCM	Variable conductance mode

56 ***Subscripts***

57	cp	Cold plate
58	cw	Cooling water
59	e	Evaporator
60	in	At inlet
61	loss	heat loss
62	out	At outlet
63	vd	Voltage drop loss

64 **1. Introduction**

65 With the ever-increasing number of on-board electronic devices, the power level and the
66 component integrated density become larger and larger. It is recognized that the localized heat
67 flux of the component can be up to 100 W/cm^2 . It is, therefore, imperative to develop new
68 techniques to remove the heat dissipation from the avionics since the capability of the typical
69 cooling system is insufficient. Nowadays, among cooling techniques for electronic devices,
70 loop heat pipes (LHPs) are considered as one of the most attractive ways to achieve high
71 efficiency of heat transfer [1, 2].

72 LHPs utilize the vapor-liquid phase change of the working fluid to transport the heat
73 between the evaporator and the condenser. The circulation of the fluid is driven by the capillary
74 forces developed in the porous wicks. The advantages of the flexibility, temperature control
75 and heat transport capability can make LHPs extend to the applications of terrestrial
76 surroundings, aircraft, submarine and high-speed railway [3-6]. Over the past two decades, a
77 large number of experimental, theoretical and numerical simulation studies on LHPs have been
78 reported to provide useful data to comprehensively understand the physical mechanisms under
79 various operating conditions and to optimize their design [7-10].

80 In terrestrial gravity environment, the relative position of different components will
81 significantly influence the liquid-vapor distribution and bubble movement in the loop due to
82 the effect of the gravity, which induces different startup behaviors and steady-state operating
83 performances of the LHP [11, 12]. Compared to conventional LHP with a single compensation
84 chamber (CC), the dual compensation chamber loop heat pipe (DCCLHP) was developed by
85 configuring two CCs on the two ends of the evaporator to achieve the liquid supply for the
86 primary wick under any orientation in terrestrial gravity.

87 It appears from the previous investigations that there are quite few reports on the operating
88 performance of DCCLHP. Gerhart and Gluck [13, 14] designed a DCCLHP and verified that it
89 could work successfully at different orientations. Their experimental results showed that the
90 heat transfer coefficient and operating temperature were evidently different in different
91 evaporator and CCs orientations. Wolf and Bienert [15] investigated the effect of the relative
92 elevation of the evaporator and condenser on the temperature control characteristics of the
93 conventional LHP and DCCLHP. It was found that the operating temperature increased as the

94 evaporator was elevated above the condenser. Long and Ochterbeck [16] experimentally
95 studied the influence of the transient cyclic heat loads and orientations on the performance of a
96 DCCLHP. They found that the startup temperature overshoot augmented with the increase of
97 the tilt of evaporator and it had a similar performance under both constant heat load and cyclic
98 heat load with the frequency being more than 0.1 Hz. Lin et al. [17] also designed a DCCLHP
99 and confirmed the normal operating at any orientations. However, the operating performance
100 was different under different orientation conditions. Bai et al. [18] experimentally studied the
101 startup behavior for a DCCLHP with insufficient inventory and found that it could still start up
102 at 5 W but the temperature overshoot sometimes was large. They considered that the different
103 startup behaviors resulted from the variation of the liquid-vapor distribution and the heat leak
104 from the evaporator to the CCs. In addition, they also investigated the temperature hysteresis,
105 reverse flow and temperature oscillation. Lin et al. [19] carried out visual observations of the
106 flow inside the DCCLHP and studied the start-up behavior, operating characteristics and
107 instability. They presented detailed analyses to give insight into the operating mechanism based
108 on the observations. Chang et al. [20] designed a DCCLHP with the visualization of CCs for
109 the aircraft anti-icing system and carried out the experimental investigation on the thermal
110 performance. They found that the DCCLHP could start up successfully with the heat loads
111 from 10 W to 180 W. The angle of attack could affect the operating temperature significantly
112 and cause temperature oscillations of the whole system.

113 However, the on-board electronic devices always suffer from a variety of acceleration forces
114 when the fighter aircraft maneuvers and combats. The effect of the acceleration forces will
115 change the performance of the cooling devices. For instance, the LHP could not start up or
116 reach a steady state because the liquid working fluid wasn't able to sufficiently wet the
117 capillary wick under such an acceleration field. Currently, there are only a few literatures
118 which present the operating characteristics of the conventional LHP and DCCLHP. For the
119 startup behavior and operation performance of a miniature aluminum-ammonia LHP in
120 elevated acceleration environment, the impact of varying heat load, acceleration magnitude
121 (from 0 g to 4.8 g) and direction was experimentally studied by Ku et al. [21, 22]. Their results
122 depicted that the LHP could normally start up but temperature fluctuation happened under
123 some acceleration conditions. Fleming et al. [23] experimentally investigated the effect of

124 different evaporator heat inputs (from 100 to 600 W) and radial accelerations (from 0 to 10 g)
125 on the performance of a titanium-water LHP. It was found that dry-out conditions happened
126 more readily at from 100 to 400 W and the reprime could be obtained after an acceleration
127 event. The radial acceleration had little effect on the evaporative heat transfer coefficient and
128 thermal resistance of the LHP. But the evaporator wall superheat was higher at steady state
129 elevated accelerations comparing with 0 g. Yerkes et al. [24] carried out experimental studies
130 on the transient operating characteristics of a titanium-water LHP under combined constant
131 heat load and steady-periodic acceleration fields. Radial acceleration peak-to-peak values and
132 frequency of the sine wave ranged from 0.5 g to 10 g and 0.01 Hz to 0.1 Hz, respectively. The
133 heat load ranged from 300 W to 600 W. The results showed that the less detrimental influence
134 there was on the LHP performance under the effect of higher acceleration frequencies and
135 peak-to-peak amplitudes. Conversely, decreased acceleration frequency and increased
136 peak-to-peak amplitude appear to have a greater detrimental impact on the LHP performance.
137 Later on, the transient operating performance of a titanium-water LHP subjected to a
138 phase-coupled evaporator heat input and acceleration field was discussed [25]. Both evaporator
139 heat inputs (from 100 W to 700 W) and radial accelerations (from 3 g to 10 g) were generated
140 as periodic sine wave at the frequency of 0.05 Hz. Their phase angles were set to 0° , 180° and
141 270° . It was found that the phase angle and condenser temperature could affect the time of LHP
142 operating failure. This was partially due to the natural frequency of the fluid motion inside the
143 condenser, which was effected by the induced forces resulting from the driving frequency of
144 the acceleration coupled to the frequency of the heat input. Xie et al. [26] conducted
145 experimentally investigation on the operating performance of a DCCLHP under terrestrial
146 gravity and elevated acceleration conditions. The effect of the acceleration could be regarded
147 either as an additive heat load or as a cold load. The transition of the operation mode was the
148 function of the acceleration direction, magnitude and heat load.

149 To the best knowledge of the authors, there are no detailed data available in the open
150 literatures on the effect of the acceleration forces on the operating characteristics of the
151 DCCLHP. Hence, the objective of the present study is to provide a comprehensive
152 experimental data exploring the transient operating performance of a DCCLHP subjected to
153 variable heat loads and radial acceleration forces. In the current study, the evaporator heat load

154 and acceleration force are applied at the same time. Three different directional acceleration
155 configurations at different acceleration magnitudes (up to 11g) are taken into account.

156 **2. Experimental apparatus**

157 In the current work, an experimental test rig that is used to investigate the transient operating
158 performance of a DCCLHP subjected to acceleration forces was constructed at the Reliability
159 and Environmental Engineering Laboratory at Beihang University, Beijing, China.

160 *2.1 Experimental setup*

161 The diagram of the experimental system is schematically shown in Fig. 1, which mainly
162 consists of acceleration simulating and control subsystem, water cooling circulation subsystem,
163 data acquisition and control subsystem as well as test section. The main components of the
164 water cooling circulation subsystem include a gear pump, mass flow meter (DMF-1-2),
165 thermostatic water tank, plate heat exchanger and cold plate. The thermostatic water tank kept
166 the cooling water at 19 °C. The gear pump drove the cooling water circulating in the loop,
167 which was regulated by a variable-frequency driver. Accurate flow measurement was
168 accomplished by the mass flow meter based on Coriolis force with an accuracy of $\pm 0.5\%$. The
169 cooling water absorbed the heat inside the aluminum cold plate (type 6061) and then entered
170 the plate heat exchanger, in which it was cooled to a low temperature. Then the cooled water
171 recycled back to the thermostatic water tank.

172 The data acquisition and control subsystem is mainly composed of a computer, data
173 acquisition instrument (Agilent 34970A), resistance temperature detectors (RTDs) Pt100,
174 electric resistance heater and precision DC power supply. The flexible polyimide film electric
175 resistance heater was adhesively attached to the outer surface of the evaporator to apply the
176 heat load. The range of 0-400 W can be adjusted by both altering the output voltage and current
177 of the DC power supply (DH1716A-13) ranged from 0 to 250 V and from 0 to 5 A, respectively.
178 The temperatures at all test points and the mass flow rate were recorded by the Agilent 34970A
179 and saved in a remote computer located in the control room.

180 In the acceleration simulating and control subsystem, the acceleration force was created by
181 spinning clockwise of the rotary arm of the centrifuge, which was driven by an electric motor.
182 When the centrifuge operated, the radial acceleration up to 11g could be generated at the end of
183 the rotary arm. The continuous operation for no more than an hour was required because of

184 safety concerns. The acceleration controller could regulate the rotational velocity of the
185 centrifuge with an accuracy of $\pm 5\%$ of the given value. The liquid collecting rings and the
186 electric slip rings installed in the centrifuge axis well linked up the stationary and rotational
187 parts of the cooling water tubes, signal wires and electric wires for heating, respectively. They
188 kept the liquid flow and the electric current working properly. A photo of the centrifuge and the
189 test section mounted on the rotary arm was shown in Fig. 2.

190 In the current work, a stainless steel-ammonia DCCLHP with insufficient fluid inventory,
191 which means the evaporator core could not be filled fully with liquid under all conditions, was
192 manufactured in the China Academy of Space Technology. Fig. 3 illustrates a picture of the
193 experimental DCCLHP and the detailed construction of the evaporator and the CCs. The
194 outline size of the DCCLHP is 565 mm \times 469 mm \times 25 mm. A primary nickel wick with a pore
195 radius of 1.5 μ m was housed in the evaporator envelope. In order to route the gas and vapor
196 bubbles out of the evaporator core at any orientation, the bayonet was present and extended to
197 the middle point of the evaporator core. The liquid and vapor transport lines as well as
198 condenser line were all stainless steel smooth-walled tubes with an outer diameter of 3.0 mm.
199 Table 1 shows a summary of the major design parameters of the experimental DCCLHP. The
200 condenser line was welded to several cooling copper fins which were mounted on the top side
201 of the cold plate with thermal conductive grease. All the components of the DCCLHP were
202 wrapped with insulation materials and installed in a stainless steel enclosure, which was
203 crammed with glass wool for thermal insulation.

204 Non-uniform radial acceleration forces for the whole enclosure were induced when the test
205 section assembly was mounted on the end of the rotary arm. In order to meet the requirement
206 of GB/T 2423.15, the acceleration magnitude should range from 90% to 130% compared to the
207 value at the center over the test section. This could be accomplished by changing the setting
208 value of the rotating radius of the centrifuge.

209 In the current work, sixteen RTDs were used to monitor the temperature profile in the
210 experiment. Fig. 4 schematically presents the positions of the RTDs along the loop, which was
211 placed horizontally on the rotary arm. RTD1 and RTD2 were attached on the top and bottom of
212 the CC1 outer surface, respectively. RTD3, RTD4 and RTD5 were located on the evaporator.
213 RTD 6 and RTD7 were attached on the top and bottom of the CC2 outer surface, respectively.

214 The cooling water temperatures at the inlet and outlet of the cold plate were measured by
215 directly submersed RTD14 and RTD15, respectively. RTD16 was used to monitor the ambient
216 temperature.

217 *2.2 Calibration and validation*

218 Prior to the formal experiment, calibrations of the RTDs were carried out over two
219 temperature ranges on the basis of the estimated operating temperature. During the calibration,
220 a constant-temperature bath was used to obtain the required temperature range. A standard
221 platinum RTD with a resolution of ± 0.01 °C was utilized to compare the temperatures from the
222 sixteen RTDs. When the bath reached a steady state at a given temperature, sixteen readings
223 were sampled and the bath temperature was changed. Both cooling water temperatures at the
224 inlet and outlet of the cold plate, as well as ambient temperature were calibrated in the range of
225 12 to 30 °C in 2 °C intervals. The other RTDs located on the loop were calibrated over the
226 whole range of 12 to 60 °C in 2 °C intervals. In both estimated temperature ranges, temperature
227 increment from the lowest to the highest value and decrement from the highest to the lowest
228 value were conducted, respectively. The average reading at a given set-point temperature was
229 determined based on the achieved two groups of data.

230 The mass flow meter used in the cooling water loop was calibrated to calculate accurately
231 the amount of dissipate heat from the DCCLHP. When the water in the thermostatic water tank
232 reached a steady temperature of 20 °C, the flow in the cooling water loop was diverted to a
233 measuring device by a three-way valve installed after the flow meter. As the time span got to a
234 specified amount of time of 360 s, the voltage from the flow meter and the mass were recorded.
235 The mass flow rates were in the range of $m=10$ kg/h to 50 kg/h in intervals of approximate
236 10kg/h. Finally, the relationship between the output voltage and the mass flow rate can be
237 achieved.

238 In order to verify the validation of the experimental setup, the measurement of thermal
239 conductivity of a pure copper bar with the diameter of 30 mm was conducted under terrestrial
240 gravity conditions. Heat load was applied at the end of the copper bar by a circular electric
241 resistance heater. A simple copper cold plate heat exchanger was manufactured and the other
242 end of the bar can be embedded in a circular groove in the cold plate. The cooling water
243 absorbed the heat transmitted from the bar. Two RTDs were located at the inlet and outlet of

244 the heat exchanger to monitor the change of cooling water. The other two RTDs at a distance of
245 60 mm were attached to the outer surface of the bar to record its temperature. In the test, the
246 cooling water in the tank was kept at 20 °C and ambient temperature was 20.1°C. The flow rate
247 was 3.31kg/h. The whole test section was wrapped with insulation materials to minimum heat
248 loss from the surface to the ambient.

249 When a steady state reached, the thermal conductivity λ could be calculated by the Fourier's
250 law:

$$251 \quad \lambda = Q_{cw}L / A\Delta T \quad (1)$$

252 where Q_{cw} is the heat extracted to the cooling water, L is the distance between two RTDs
253 locations on the bar, ΔT is the temperature difference between two RTDs located on the bar, A
254 is the bar section area.

255 Comparison with the known value from Yu [27] was made based on the obtained test data
256 and the test relative error of the thermal conductance was 8.4%.

257 **3. Experimental procedure and uncertainty analysis**

258 The following presents the experimental procedure, heat loss calculation for experimental
259 setup, test data process and uncertainty analysis.

260 *3.1 Experimental procedure*

261 Prior to each experiment, the test section enclosure was mounted horizontally at the proper
262 location on the rotary arm according to the given acceleration direction. Three different
263 directions of the acceleration, namely configuration A, B and C, were employed in the present
264 work, as shown in Fig. 5. For the cases of configuration A and B, the axis of the evaporator and
265 CCs was consistent with the direction of the radial acceleration. The liquid line was placed at
266 the outer edge of the rotary arm for configuration A and at the inner edge for configuration B.
267 For configuration C, the axis of the evaporator and CCs placed at the outer edge was
268 perpendicular to the direction of the radial acceleration.

269 Firstly, the data acquisition and control subsystem and water cooling circulation subsystem
270 were turned on in turn. The cooling water started circulating flow until the whole system
271 reached a steady state. Then the startup time of the centrifuge was set to 30 s which was the
272 time required for the acceleration to reached a set value. Switch on the power supply for the
273 heater while starting the centrifuge to applying the thermal load and acceleration force at the

274 same time. A series of experiments were firstly carried out in terrestrial gravity to achieve the
275 basic operating behavior of the DCCLHP. Then the effect of different magnitudes and
276 directions of the acceleration, as well as heat loads on transient operating performance was
277 investigated.

278 In the current study, six different heat loads ($Q_e=25$ W, 80 W, 150 W, 200 W, 250 W, 300 W)
279 and five radial acceleration magnitudes ($a_r=3$ g, 5 g, 7 g, 9 g, 11 g) were taken into account. It
280 needs to be noted that the gravity is always present in all experiments. The continuous
281 operating time of the centrifuge could not exceed 1 hour for safety. The cooling water
282 temperature at the inlet of the cold plate was kept from 19.8 to 20.8 °C. The surroundings
283 temperature of the centrifuge room was maintained from 25.6 to 27.5 °C by air conditioning.

284 3.2 Heat loss calculation

285 The total power, which was the product of the voltage and current output from the precision
286 DC power supply, consisted mainly of the following three parts. The first part was the voltage
287 drop power loss caused by the resistance of the wires themselves. The wire length was more
288 than 15 m between the heater and the control room, which led to non-negligible voltage drop.
289 The power loss could be achieved by multiplying the voltage drop and the current. The second
290 was the heat loss. Because the surface temperatures of the evaporator, CCs and transport lines
291 were larger than the surrounding temperature in general, thermal transport from these
292 components to the surroundings contributed to the heat loss. The third part was the heat
293 extracted to the cooling water, which was the primary heat input on the evaporator. Therefore,
294 the heat loss Q_{loss} could be calculated approximately by the following expressions.

$$295 \quad Q_e = UI - Q_{\text{vd}} \quad (2)$$

$$296 \quad Q_{\text{loss}} = Q_e - mc(T_{\text{out}} - T_{\text{in}}) \quad (3)$$

297 Where U and I are the voltage and current output from power supply, respectively, Q_{vd} is the
298 voltage drop power loss, m is the mass flow rate of the cooling water, c is the specific heat
299 capacity, T_{in} is the inlet temperature of the cold plate, T_{out} is the outlet temperature of the cold
300 plate.

301 In all experiments, the maximum value Q_{loss}/Q_e was not more than 16.7%.

302 3.3 Uncertainty analysis

303 The uncertainty of the physical quantity R , which was a function of the measured variables

304 x_1, x_2, \dots, x_i , could be calculated by the following expression [28].

$$305 \quad \frac{U(R)}{R} = \left(\sum_{i=1}^n \left(\frac{1}{R} \frac{\partial R}{\partial x_i} \delta x_i \right)^2 \right)^{1/2} \quad (4)$$

306 where δx_i denotes the uncertainty of the i th measured variable.

307 In the present work, the thermal conductance of the DCCLHP was determined by the
308 evaporator temperature and the cold plate temperature:

$$309 \quad G = Q_e / (T_e - T_{cp}) \quad (5)$$

310 where G is the thermal conductance, T_e is the evaporator temperature, T_{cp} is the average
311 temperature of the cold plate, which can be calculated by Eq. (6):

$$312 \quad T_{cp} = 0.5(T_{out} + T_{in}) \quad (6)$$

313 As taking into account the effect of the RTDs, electric wire, slip rings, junction terminal and
314 data loggers, the accuracies of the temperature measurements were approximately ± 0.5 °C. The
315 maximum uncertainty of the temperature was 2.6%. The maximum uncertainty of the voltage
316 and current was 4.6% and 2.9%, respectively. As a result, the maximum uncertainty of the heat
317 load was 5.4%. According to Eq. (5) and (6), the maximum uncertainty of the thermal
318 conductance was approximately 10.5%.

319 **4. Results and discussion**

320 The following sections will address both the startup and operating characteristics of the
321 DCCLHP as it was subjected to different acceleration directions, acceleration magnitudes and
322 heat loads on the evaporator based on a series of experiments.

323 *4.1 Effect of the acceleration directions*

324 Fig. 6 illustrates the loop temperature profiles at 5 g and 25 W for configuration A, B and C.
325 Fig. 7 schematically shows the estimated vapor-liquid distributions in the loop subjected to the
326 acceleration force for the three configurations. During the experiment, the whole procedure
327 could be divided into three phases: the terrestrial steady phase, the acceleration phase and the
328 unloading phase. In the terrestrial steady phase, the DCCLHP is operated at a steady state with
329 the effect of the cooling water. The acceleration force and the heat load are applied during the
330 acceleration phase, whereas the acceleration force is removed in the unloading phase.

331 As can be seen clearly in Fig. 6, the temperature profiles of the loop under configuration A,

332 B and C show quite different behaviors. For the case of configuration A, the temperature varies
333 slowly within the first 250 s, whereas a temperature peak value occurs at approximate 200 s for
334 both configurations B and C. In Fig. 6(a), it is at 169 s that both acceleration force and heat
335 load are applied simultaneously. The temperature of the evaporator and CC1 (RTD1 and RTD2)
336 rises immediately when the heat load is applied to the evaporator. The RTD8 temperature at the
337 outlet of the vapor line also steeply increases from 22.2 °C to 24.4 °C nearly at the same time.
338 It could be explained by the fact that the evaporation occurred and the vapor existed in the
339 evaporator grooves at the very beginning. Compared to the temperature rise of RTD4 and
340 RTD8, the temperature for both the condenser (RTD9 and RTD10) and the liquid line inlet
341 (RTD11) decreases approximately 1 °C. Especially for the liquid line, the temperatures of
342 RTD12 and RTD13 show a very steep drop at 173 s. This indicates that the subcooling liquid
343 from the condenser reaches the outlet of the vapor line and the positive fluid circulation starts.
344 Therefore, the startup is deemed a success and the startup time is approximately 4 s.

345 When the acceleration force is applied, the vapor-liquid distribution is changed due to the
346 force effect, as shown in Fig. 7(a). The liquid of the working fluid in the CC1 and evaporator
347 core will be pushed into the CC2. As a result, the level of the liquid in the CC1 reduces to the
348 evaporator core, but the level in the CC2 rise above it. This distribution will result in the
349 increase of the heat leak from the evaporator to the CC1 and decrease to the CC2. Therefore,
350 the CC1 temperature increases obviously. The CC2 temperature starts to drop until 199 s due to
351 the returning liquid cooling. Under the effect of the acceleration force during the initial period,
352 the liquid with lower temperature in the condenser flows through the right bends of U-shaped
353 coils and easily enters the liquid line and goes back to the evaporator. Consequently, the
354 temperature from RTD9 to RTD13 drops. With the increase of the condensation temperature in
355 the condenser, the temperature from RTD9 to RTD13 rises in turn. As an equilibrium state of
356 the loop reaches finally, the temperature of the evaporator, CC1 and CC2 are 25.2 °C, 24.8 °C
357 and 21.7 °C, respectively.

358 In the unloading phase, the gravity will make the liquid in the CCs and evaporator core to be
359 in the same level again. It is noted that the heat leak from the evaporator to CC2 increases.
360 Therefore, the CC2 temperature shows a steep rise with the increase of the evaporator
361 temperature. In the current work, the operating performance after unloading the acceleration

362 force will not be discussed here in detail.

363 For the case of configuration B, as demonstrated in Fig. 6(b), the evaporator temperature
364 shows a steep rise as the heat load is supplied at 63 s. The RTD8 temperature increases
365 approximately 0.4 °C. In the meantime, the temperature of RTD9, RTD10 and RTD11 changes
366 slightly. Nevertheless, the RTD12 and RTD13 temperature shows no obvious changes. The
367 reason could be that the fluid flow in the external loop is driven by the acceleration force. Since
368 the radial acceleration force is small and the tangential acceleration force will dominate during
369 the initial period, the liquid with lower temperature in the coils of the condenser is driven to
370 pass through the right U-shaped bends and then enters the liquid line.

371 However, it is almost at 69 s that the RTD8 temperature begins to decrease rapidly and the
372 RTD13 temperature increase remarkably, as well as both RTD9 and RTD10 temperatures
373 decrease sharply. It is noted that the RTD11 temperature increases dramatically starting from
374 71 s. The RTD12 temperature shows a steep rise until 83 s. The reason could be attributed to
375 the contribution of the following coupled with Fig. 7(b). When the radial acceleration force
376 dominates, both the vapor phase and liquid phase are redistributed in the loop due to the effect
377 of the acceleration force. Moreover, it is likely that the evaporation occurred in the evaporator
378 core. The liquid will be pushed from the CC2 and evaporator core into CC1 and the vapor
379 floats into the CC2, even reversely get into the liquid line via the bayonet. As a result, the heat
380 leak from the evaporator to the CC2 increases but decreases to the CC1. There is a slight rise
381 for both RTD1 and RTD2 temperature and a sharp rise for both RTD6 and RTD7 temperature
382 with almost the same value. The reverse of the vapor in the liquid line results in the increase of
383 the RTD12 and RTD11 temperatures. The liquid from the condenser entering the vapor line
384 leads to the drop of the RTD8 temperature.

385 It is found that at 139 s the RTD8 temperature shows a very steep rise from 21.0 °C to 30.3
386 °C. This demonstrates that the evaporation occurs in the evaporator grooves and the vapor
387 arrives at the outlet of the vapor line. The RTD11 temperature decreases rapidly at the same
388 time. Then the RTD 12 temperature drops dramatically after 141 s while the RTD13
389 temperature drops after 143 s. At this moment, the circulation flow forms and the DCCLHP
390 starts up. After the evaporator temperature reaches the highest of 31.7 °C at 183 s, the
391 temperatures of the evaporator, CC2 and vapor line decrease to a constant value gradually. It is

392 believed that the entire loop reaches an equilibrium state at 2400 s. The temperatures of the
393 evaporator, CC1 and CC2 at the steady state are 25.5 °C, 25.3 °C and 24.6 °C, respectively. In
394 the unloading phase since 2800 s, the evaporator temperature drops slightly and then increases.

395 In addition, the RTD9 temperature increases suddenly and begins to oscillate at 1125 s. The
396 RTD13 temperature also oscillates simultaneously but the temperatures of the RTD10, RTD11
397 and RTD12 show no oscillation. Furthermore, this oscillation sustains approximately 650 s and
398 disappears. This phenomenon may not be explained clearly now but will be further studied in
399 the future work.

400 According to the temperature profiles shown in Fig. 6(c), it is recognized that the
401 temperatures of the evaporator and CCs increase as the heat load is applied at 85 s. But the
402 temperatures of the condenser and transport lines show no apparent variations before 95 s. It is
403 at 95 s that the RTD11 and RTD13 temperatures increase significantly. It could be the reason
404 that the tangential acceleration force changes the vapor-liquid distributions in the loop during
405 the initial period of the centrifuge rotating. A portion of liquid is pushed into the CC1 from the
406 CC2 and evaporator core, where the vapor-liquid distribution is illustrated in Fig. 7(c). It could
407 be explained by the fact that there exist bubbles in the evaporator core or the vapor occurs
408 inside of the wick and the evaporation happens in the evaporator core prior to the vapor
409 grooves. The vapor through the bayonet flows into the liquid line. As a result, the RTD13
410 temperature increases rapidly. In the condenser, the liquid could gather in the left U-shaped
411 bends due to the effect of the tangential acceleration force. And there is no massive fluid flow
412 into or out of the condenser. Therefore, the temperatures of the RTD8, RTD9, RTD10 and
413 RTD11 show no obvious changes. However, the RTD8 temperature begins to drop at 101 s. It
414 is indicated that the liquid reversely flows into the vapor line from the condenser. It is worth to
415 note that the RTD12 temperature shows a very small change before 165 s as the RTD11 and
416 RTD13 temperature increases significantly. The reason could be that the annular flow is formed
417 in the liquid line due to the effect of the radial acceleration force. A thin liquid layer prevents
418 the wall temperature from increasing until it completely evaporates to the vapor.

419 At 167 s, the RTD8 temperature reaches the minimum value of 22.1 °C and the RTD11
420 temperature gets to the maximum value of 24.8 °C. Afterwards, the RTD8 temperature
421 increases quickly and the RTD11 temperature drops. This shows that the vapor via the vapor

422 line enters the condenser and then flows into the liquid line. It is at 171 s that the peak
423 temperatures of the RTD4 and RTD13 reach 31.0 °C and 30.0 °C, respectively. According to the
424 variation of the external loop temperatures, the DCCLHP starts up after 82 s since the heat load
425 is applied.

426 After 171 s, the temperatures of the evaporator, vapor line and CCs drop gradually. But the
427 condenser temperature increases slowly and then drops. The liquid line temperature decreases
428 rapidly to a constant and then increases quickly. When the time is 791 s, the DCCLHP reaches
429 a thermal equilibrium state and the final operating temperature is 23.6 °C. It is obviously
430 different with the cases of configuration A and B that the whole loop temperatures ranges from
431 22.8 °C to 23.6 °C, which are higher than the sink temperature but lower than the ambient
432 temperature. The above phenomenon can be explained as the following. Under configuration C,
433 the effect of the acceleration force is similar to the gravity-assisted effect. After the DCCLHP
434 starts up, the capillary pressure difference across the wick exceeds the total loop pressure drop
435 since the effect of the acceleration force promotes the subcooling liquid returning to the
436 evaporator. Therefore, the capillary pressure difference decreases and the relevant temperature
437 difference also decreases in order to balance the total loop pressure drop. This reduces the heat
438 leak, which causes the decrease of the operating temperature. Moreover, the loop pressure
439 equilibrium does not reach if the capillary pressure difference reduces to 0 Pa. The acceleration
440 force will drive the working fluid circulating in the loop. Consequently, a two-phase flow
441 occurs in the vapor line and both the vapor and the liquid are saturated. It could be confirmed
442 that the RTD8, RTD9 and RTD10 temperatures are almost equal. In addition, it is likely that
443 the actual liquid evaporation area is reduced by the effect of the acceleration force under this
444 configuration. This could also lead to the decrease of the evaporation temperature. In the
445 unloading phase after 2217 s, the temperatures of the evaporator and CCs increase slightly and
446 the RTD12 and RTD13 temperatures increase gently and then drop. The RTD10 and RTD11
447 temperatures decrease moderately.

448 Fig. 8 presents the loop temperature profiles at 250 W and 5 g under configuration A, B and
449 C. Partial enlarged drawings are also shown in order to see clearly the temperature variations.
450 According to the graphs shown in Fig. 8, it could be found that the RTD4 and RTD8
451 temperatures increase immediately as the heat load is applied for three different configurations.

452 This indicates that the evaporation occurs in the vapor grooves and the vapor enters the
453 condenser. The RTD11 and RTD13 temperatures drop almost at the same time. It is believed
454 that the DCCLHP starts up under configuration A, B and C. However, the loop is not able to
455 reach a steady state under configuration A during the period of the centrifuge operating. The
456 temperature oscillations occur under configuration B and a thermal equilibrium state reaches
457 under configuration C.

458 For the case of configuration A shown in Fig. 8(a), when the heat load and acceleration force
459 is applied at 57 s, the positive circulation of the working fluid starts rapidly in the loop on the
460 basis of the loop temperature changes. The liquid in the condenser is driven into the liquid line,
461 resulting in the temperatures of RTD11, RTD12 and RTD13 drops. The RTD9 and RTD10
462 temperatures near the RTD8 temperature shows that the condensing area of the condenser
463 enlarges and the subcooling of the liquid decreases. As a result, the RTD11 and RTD13
464 temperatures increase sharply after 71 s and 79 s, respectively. The condenser is completely
465 opened until the RTD11 temperature is nearly equal to the RTD10 temperature. Therefore, the
466 vapor front advanced to the outlet of the condenser, displacing the equal volume liquid toward
467 the CCs. The effect of the acceleration force changes the vapor-liquid distribution in the CCs,
468 which is similar to the results that shown in Fig. 7(a) but more liquid in the CC1. The heat leak
469 reduces from the evaporator to the CC2. Simultaneously, owing to the convection and cold
470 bayonet inside the CC2, the CC2 temperature is less than that in CC1.

471 However, it is at 355 s that the temperatures of RTD11, RTD12 and RTD13 begin to
472 decrease. This shows that the subcooling of the returning liquid increases. The RTD6 and
473 RTD7 temperatures reduce due to the cooling effect of the returning liquid. The vapor-liquid
474 interface moves back to a certain position before RTD10 point in the condenser. When the time
475 is at 1703 s, the RTD10 temperature drops suddenly. It shows that the vapor-liquid interface
476 moves back to a certain position between RTD9 and RTD10 point. The condenser is not fully
477 used. Finally, the DCCLHP fails to reach a steady state and the maximum temperature of the
478 evaporator is 40.6 °C.

479 In the unloading phase after 2815 s, the change of the vapor-liquid distribution results in the
480 heat leak increasing from the evaporator to CC2 as the acceleration force is out of action. The
481 CC2 temperature increases steeply. The temperatures of the evaporator, CC1 and vapor line

482 drop slightly and then increase slowly. But the liquid line temperatures changes a little.

483 Under configuration B, when the acceleration force and heat load are applied at 61 s, the
484 RTD8 temperature increases immediately and the RTD11 temperature drops, as shown in Fig.
485 8(b). This indicates that the vapor occurs and enters the condenser, as well as the subcooling
486 liquid from the condenser flows into the liquid line. It is at 67 s and 71s that the RTD11 and
487 RTD13 temperatures begin to increase sharply, respectively. With the aid of the CC1 and CC2
488 temperatures, it is believed that the CC1 is almost full of the cooling liquid and the CC2 is
489 filled with a large amount of vapor under the effect of the acceleration force. Therefore, the
490 heat leak from the evaporator to CC1 is small whereas to CC2 is large. The RTD1 and RTD2
491 temperatures show a slight rise but the RTD6 and RTD7 temperatures increase rapidly.

492 With the input of the heat load, the loop temperatures except for CC1 begin to oscillate at a
493 certain time after 110 s and the amplitude become larger and larger gradually. It is difficult to
494 determine which component first starts to oscillate. Perhaps both CC2 and condenser show
495 oscillation simultaneously. It is on the liquid line that the amplitude of the periodic temperature
496 oscillation suddenly become larger after approximate 380 s and is larger than that of the other
497 components. Moreover, the amplitudes of RTD11, RTD12 and RTD13 enlarge in turn.
498 According to the periodic temperature oscillation, a persistent forward and reverse liquid flow
499 in the liquid line does alternate as evidenced by the temperatures of the liquid line inlet
500 (RTD11) and outlet (RTD13). The RTD11 and RTD13 temperatures oscillate between 25.7 °C
501 and 30.2 °C, as well as 25.6 °C and 31.4 °C, respectively. The RTD11 and RTD13 temperatures
502 oscillation has a nearly same period of 144 s. However, it is clearly seen that the RTD13
503 temperature oscillation pattern is not symmetric. It takes around 94 s to drop from the peak
504 temperature to the valley, and 50 s to rise from the valley temperature to the peak. The
505 oscillating temperature shows a similar change for the CC2, evaporator and condenser. Finally,
506 a quasi-stable state is established where the peak and valley for the evaporator and CC2
507 temperatures are 35.4 °C and 34.4 °C, as well as 33.3 °C and 32.3 °C, respectively. Their
508 temperature oscillation periods are both around 120 s. After the acceleration force is unloaded
509 at 2020 s, the evaporator and CCs temperatures rise sharply but the liquid line temperature
510 drops.

511 The underlying physical mechanism during the temperature oscillations and the interactions

512 among the DCCLHP various components could be explained as the following. When the
513 RTD11 temperature begins to drop from the peak, the vapor front would go back to the
514 condenser and recede gradually. Since additional liquid from the CCs via the bayonet is used to
515 replenish the space left by the vapor recession, the liquid flow in the liquid line would reverse.
516 Under this situation, the reverse liquid flows in the liquid line and the forward vapor flows in
517 the vapor line, both are existed simultaneously. As the liquid recedes inside the condenser, the
518 acceleration pressure head would increase. In order to balance the loop pressure, the capillary
519 pressure difference increases which requires the CC2 temperature to rise. The loop pressure is
520 balanced as the CC2 temperature reaches its peak value. In the meantime, the evaporator
521 temperature also increases and reaches its peak value. Consequently, the vapor front stops
522 receding and starts to advance. At the same time, the liquid length inside the condenser reaches
523 its maximum as well. When the front goes forward and arrives at some point in the condenser,
524 the RTD11 temperature falls to its valley value. As soon as the front advances, the acceleration
525 pressure head decreased. The relevant capillary pressure difference decreases to balance the
526 loop pressure. As a result, the CC2 temperature drops and the evaporator temperature drops
527 following the CC2. As the front advances, the subcooling of the liquid from the condenser
528 reduces. This results in the RTD11 temperature increases. It would reach the peak value until a
529 certain time after the vapor-liquid front rushed out of the condenser. The front rushing out
530 could be due to the insufficient inventory of the working fluid and the flow inertia effect as
531 well. When the subcooling of the returning liquid could not balance the heat leak, the CC2
532 temperature stops falling and starts to rise. This starts the next cycle of the loop rise and fall
533 above.

534 However, it is very difficult to completely explain the fluid flow and temperature oscillations.
535 It could be the reason of the complexity and instability of the two-phase flow and heat transfer,
536 impacted by many coupled factors such as the acceleration force, degree of subcooling, heat
537 load and mass flow rate. It is also related to the adaptation of the CCs volume and the fluid
538 inventory. Temperature oscillation is undesirable because of the deleterious effects on the
539 precise temperature control in practical application. Therefore, it is extremely essential that the
540 oscillation mechanism is further investigated.

541 As can be clearly seen from Fig. 8(c), the RTD8 temperature increases immediately as soon

542 as the head load is applied at 141 s under configuration C. The vapor reaches the outlet of the
543 vapor line. As opposed to the RTD8, the temperatures of the condenser and liquid line drop and
544 then increase rapidly. It is at 149 s and 153 s that the temperatures of RTD11 and RTD13
545 increase, respectively. Because the vapor-liquid distributions in the CCs and evaporator core
546 caused by the acceleration force is similar to that under the terrestrial gravity, both CC1 and
547 CC2 temperatures increase. This distribution is different with that under configuration A and B.
548 After 207 s, the RTD11, RTD12 and RTD13 temperatures show a momentary oscillation and
549 then decrease to a constant value. In the condenser, the RTD9 and RTD10 temperatures near
550 the RTD6 temperature are much higher than the RTD11 temperature. This means that the
551 vapor-liquid interface locates at some point in the condenser, and the condenser is not fully
552 used. It is believed that the DCCLHP reaches a steady state at 2000 s. At the steady state, the
553 evaporator temperature is approximate 36.9 °C. The RTD6 and RTD7 temperatures are 35.5 °C
554 and 34.9 °C, respectively. Both RTD1 and RTD2 temperatures are close to 35.2 °C. After the
555 centrifuge stops at 2770 s, the evaporator temperature reaches 37.5 °C at a steady state. The
556 RTD6 and RTD7 temperatures are 35.5 °C and 30.3 °C, respectively. The RTD1 and RTD2
557 temperatures are close to 35.6 °C.

558 Compared the profiles shown in Fig. 6 with those in Fig. 8, it can be found that the startup
559 behavior of the DCCLHP is susceptible to the direction of the acceleration force at a small heat
560 load of 25 W. The evaporation inside the core and the reverse flow in the external loop could
561 happen under configuration B and C. At a larger heat load of 250 W, the DCCLHP is able to
562 start up quickly under different configurations. But whether the DCCLHP can reach a steady
563 state is dependent on the acceleration direction. Moreover, the periodic temperature oscillation
564 and reverse liquid flow occurs under configuration B.

565 Fig. 9 depicts the operating temperature and thermal conductance at different heat loads
566 under three different configurations and terrestrial gravity as the acceleration magnitude is 5 g.
567 Note that the evaporator temperature ascends continuously and the loop fails to reach a steady
568 state during the given time for these cases of 25 W, 80 W and 150 W in terrestrial gravity as
569 well as 150 W, 200 W and 250 W at 5 g under configuration A. The maximum value of the
570 evaporator temperature is used instead of the steady operating temperature for the comparison.

571 As can be seen in Fig. 9(a), quite different behavior on the operating temperature is shown

572 under different configurations and terrestrial gravity as the heat load is less than 200 W, but had
573 a small difference at a larger heat load of 300 W. The operating temperatures are 45.7 °C, 40.0
574 °C and 38.5 °C under terrestrial gravity when the heat load is 200 W, 250 W and 300 W,
575 respectively. The operating temperatures at 300 W under configuration A, B and C are 37.6 °C,
576 38.4 °C and 39.0 °C, respectively. Under terrestrial conditions, the DCCLHP has a higher
577 operating temperature than that under acceleration conditions. When the heat load ranged from
578 150 W to 300 W, there is a small difference of the operating temperature at a fixed heat load
579 between under terrestrial gravity and under configuration A.

580 For configuration A at 5 g, the steady state reaches for the cases of 25 W, 80 W and 300 W
581 and the operating temperatures are 25.2 °C, 38.6 °C and 37.6 °C, respectively. But it cannot
582 reach in the given time as heat loads are 150 W, 200 W and 250 W. Compared with the cases in
583 terrestrial gravity, the effect of the acceleration force promotes the DCCLHP operating under a
584 small heat load. However, the reverse effect occurs at a moderate heat load. For the cases of
585 configuration B and C at 5 g, the DCCLHP can reach a steady state and has a lower operating
586 temperature. When the heat load is no more than 150 W, the operating temperature under
587 configuration B is larger than that under configuration C. However, the opposite happens as the
588 heat load is no less than 200 W.

589 In Fig. 9(b), it is seen that the thermal conductance at 5 g generally shows a trend of increase
590 with the increase of the heat load under acceleration and terrestrial conditions. For the thermal
591 conductance at a fixed heat load, there is a relatively large difference among various
592 configurations and terrestrial as the heat load does not exceed 200 W, whereas a small value as
593 the heat load is not less than 250 W. When the heat load exceeds 150 W, there is nearly the
594 same thermal conductance at a fixed heat load under between terrestrial gravity and
595 configuration A.

596 In terrestrial gravity, the condenser is not fully opened as heat load is less than 300 W. The
597 DCCLHP operates at variable conductance mode (VCM). For configuration A, it operates at
598 VCM at both 25 W and 80 W and at constant conductance mode (CCM) at 300 W. For
599 configuration B, the heat loads at VCM and CCM range from 25 W to 150 W and from 200 W
600 to 300 W, respectively. For configuration C, the thermal conductance ranges from 14.7 W/K to
601 21.4 W/K. It is only at 300 W that the loop operates at CCM since the condenser is fully used.

602 To sum up, the effect of the acceleration force changes the startup behavior and operating
603 mode of the DCCLHP. The impact of the acceleration direction on the operating temperature is
604 significant at small heat load (≤ 150 W) but is weak at large heat load. The effect of the
605 acceleration direction changes the heat load range of VCM or CCM.

606 *4.2 Effect of the acceleration magnitude*

607 Fig. 10 shows the temperature profiles of the loop at 80 W under terrestrial gravity and under
608 configuration A at 5 g. As can be seen from the figure, the loop temperature shows a gradual
609 increase to its maximum value following a near steady value in terrestrial gravity. But it slowly
610 goes up to a constant value under configuration A. Under both conditions, there is an obvious
611 difference for the RTD6 and RTD7 temperatures of the CC2.

612 In Fig. 10(a), once the heat load is applied at 41 s, the RTD4 temperature augments from
613 24.3 °C to 25.2 °C. Almost at the same time, the RTD8 temperature ascends from 22.5 °C to
614 24.5 °C, which is a consequence of the vapor arrives at the outlet of the vapor line. It shows
615 that the positive circulation flow is established coupled with the drop of the temperatures from
616 RTD9 to RTD13 and the DCCLHP starts up. Because there is the same level of the liquid in the
617 CCs and core, which determines their thermal link under terrestrial conditions, the RTD1 and
618 RTD6 temperatures increase much faster than that of the RTD2 and RTD7 temperatures. From
619 90 s to 341 s, the temperatures of the evaporator, vapor line and CC1 remain almost unchanged.
620 The RTD10 temperature gradually increases to 24.0 °C until 245 s. It reveals that the vapor
621 length inside the condenser increases. It is at 369 s that the RTD10 temperature drops again,
622 which indicates the vapor-liquid interface recedes inside the condenser. As a result, the reverse
623 liquid flow in the liquid line occurs and the additional liquid from the CCs is fed to fill the
624 space in the condenser left by the recession. Therefore, the RTD13 temperature rises and then
625 drops until the positive flow starts.

626 After 343 s, the RTD1 and RTD4 temperatures augment again. It is at 403 s that the RTD9
627 temperature begins to descend, which shows the vapor-liquid interface recedes to a certain
628 point before RTD9 point in the condenser. The condenser is not fully opened. The RTD6 and
629 RTD7 temperatures are lower than that of the RTD1 and RTD2 due to the cooling effect of the
630 returning liquid. Because the evaporator temperature gets to 50.8 °C at 893 s, the heat load is
631 removed when taking the safety into consideration. Then the temperatures of the evaporator

632 and the CC1 decreases gradually but the RDT13 temperature increases rapidly.

633 For the case of configuration A, as presented in Fig. 10(b), the startup behavior is similar to
634 the case of terrestrial gravity, as shown in Fig. 10(a) during the initial approximate 20 s when
635 switching on the acceleration force at 79 s. Under this condition, the vapor-liquid distribution is
636 similar to the case as shown in Fig. 7(a). Thereby, the heat leak declines from the evaporator to
637 the CC2. In the meantime, the returning liquid with some degree of subcooling cools the fluid
638 in the CC2. Consequently, the RTD6 and RTD7 temperatures do not ascend.

639 It is at 929 s that the RTD9 temperature begins to descend quickly. It shows that the vapor
640 front recedes to some point before the RTD9 point in the condenser and the condenser is not
641 completely used. During the period from 1705 s to 2849 s, the loop remains a thermal
642 equilibrium state. The evaporator temperature is 38.6 °C and the CC1 and CC2 temperatures
643 are 38.0 °C and 23.2 °C, respectively. However, it should be noted that the evaporator and the
644 CC1 temperatures shows a rapid rise as soon as the acceleration force is unloaded at 2489 s.

645 The loop partial temperature evolutions at 300 W with four different accelerations of 3 g, 5 g,
646 7 g and 9 g under configuration B are shown in Fig. 11. Because there are similar startup
647 behaviors for all acceleration magnitudes, only the partial enlarged drawing at 3 g during the
648 initial period is shown for the purpose of brevity. For the case of 3 g, as the heat load is
649 applied at 51 s, the RTD4 and RTD8 temperatures rapidly ascend. This indicates that the vapor
650 is generated and gets to the outlet of the vapor line at larger heat load of 300 W. According to
651 the drop of the RTD10, RTD11 and RTD13 temperatures, it is believed that the DCCLHP starts
652 up.

653 As can be clearly seen from the figure, there are temperature oscillations in the loop for all
654 acceleration magnitudes. The amplitudes of the evaporator, CC2, condenser and vapor line are
655 smaller than that of the liquid line under each acceleration magnitude. As the acceleration
656 magnitude is 3 g, the amplitude and period are the largest. There are small differences of the
657 period and amplitude under 5 g, 7 g and 9 g conditions. Under all acceleration magnitudes, the
658 loop reaches a quasi-steady state finally. The valley and peak values of the evaporator
659 temperature at 3 g, 5 g, 7 g and 9 g are 36.9 °C and 37.6 °C, 38.0 °C and 38.4 °C, 37.5 °C and
660 38.0 °C, as well as 38.1 °C and 38.5 °C, respectively. The relevant periods are 28 s, 18 s, 18 s
661 and 20 s, respectively.

662 Fig. 12 shows the operating temperature and thermal conductance at 150 W, 250 W and 300
663 W under five different accelerations of 0 g, 3 g, 5 g, 7 g and 9 g for configuration B. The
664 maximum temperature is used at 150 W under terrestrial gravity since the loop fails to reach a
665 steady state. The peak value of the evaporator temperature is utilized as the temperature
666 oscillates at 250 W and 300 W under all acceleration magnitudes conditions.

667 It is found from Fig. 12(a) that the operating temperature is not susceptible to the
668 acceleration magnitude under configuration B as the heat load is large. Corresponding to the
669 case of terrestrial gravity, the effect of the acceleration force significantly reduces the operating
670 temperature, especially at 150 W. The overall trend of the operating temperature appears
671 enlargement with the increase of heat load under acceleration conditions. As the heat load is
672 150 W, the evaporator temperatures are 55.8 °C, 35.4 °C and 35.9 °C at 0g, 3g and 5g,
673 respectively.

674 As can be seen in Fig. 12(b), the thermal conductance at 250 W and 300 W is obviously
675 larger than that at 150 W under acceleration conditions. There is nearly the same value at 250
676 W and 300 W for a fixed acceleration magnitude. When the heat loads are 250 W and 300 W,
677 the thermal conductance ranges from 21.4 W/K to 22.9 W/K under acceleration conditions. In
678 addition, compared with the values at gravity terrestrial, the thermal conductance is larger
679 under acceleration conditions.

680 Fig. 13 presents the partial temperature evolutions of the loop at 80 W and five different
681 accelerations of 3 g, 5 g, 7 g, 9 g and 11 g under configuration C. As is shown in Fig. 13, there
682 is a peak for the RTD4 curve under all acceleration magnitudes. The RTD4 temperature at 3 g
683 is much larger than that at the other acceleration magnitudes. Temperature oscillations occur at
684 7 g and 9 g. The transient operating performance differs from each other and does not show an
685 obvious regularity under different acceleration magnitudes.

686 For the case of 3 g, when the acceleration force and heat load are applied at 53 s, the RTD4
687 temperature ascends immediately and RTD8 temperature also goes up steeply. This confirms
688 that the vapor from the grooves gets to the outlet of the vapor line. The quick successive drop
689 of the RTD10, RTD11 and RTD13 temperature in further indicates the positive circulation flow
690 starts and the DCCLHP starts up. For the cases from 5 g to 11 g, startup processes are similar
691 to the case of 3 g. There is a small peak for the RTD4 temperature profile during the period

692 from 140 s to 170 s. Then the temperatures of RTD4, RTD1 and RTD6 gradually increase.
693 Finally, it takes approximate 1100 s to reach the steady state. Because of the vapor-liquid
694 distribution in the CCs is similar to that shown in Fig. 7(c), the heat leaks are almost equal
695 from the evaporator to CC1 and CC2. Therefore, the RTD1 and RTD6 temperatures are nearly
696 the same. It is believed that the condenser is not fully opened according to the RTD10 and
697 RTD11 temperatures.

698 For the case of 5 g, after the DCCLHP starts up, there is a large peak for the RTD1, RTD4,
699 RTD6 and RTD8 curves. It takes approximate 800 s for the loop to reach a thermal equilibrium
700 state (the profiles do not be shown in Fig. 13). The final operating temperature is 26.7 °C. It is
701 obviously different with the cases of 3 g that the whole loop temperatures ranges from 25.3 °C
702 to 26.0 °C except for the evaporator temperature. It could be inferred that there is two-phase
703 flow in the vapor line. Furthermore, the fluid in the entire condenser could be interpreted as
704 two-phase flow. In addition, for the case of 11 g, the loop temperature distribution is similar to
705 the case of 3 g, which ranges from 25.7 °C to 26.4 °C except from the evaporator temperature
706 with 27.0 °C.

707 Under conditions of 7 g, only the RTD4 and RTD10 temperature has a slight oscillation in
708 the loop. It takes approximate 1400 s to reach the steady state. At the steady state, the RTD10
709 temperature is 2.6 °C lower than the RTD9 temperature whereas is 1.7 °C higher than the
710 RTD11 temperature. This indicates that the condenser is not completely opened. Compared
711 with the case of 7 g, the temperature oscillation of the whole loop shows more obviously at 9 g.
712 It takes approximate 136 s when the temperature oscillation starts after switching on the heat
713 load. Finally, a quasi-steady state is reached at around 1600 s and the evaporator temperature is
714 around 27.4 °C. Because the RTD11 temperature is much lower than that of the RTD9 and
715 RTD10, it means that the subcooled liquid exists in the condenser and the condenser is
716 completely used.

717 Fig. 14 depicts the operating temperature and thermal conductance at 80 W and 200 W under
718 acceleration conditions for configuration C. As is shown in Fig. 14(a), it is found that the effect
719 of the acceleration magnitude has a significant impact on the operating temperature under
720 configuration C. As the acceleration is large, the operating temperature change shows a trend of
721 decline with the increase of the acceleration magnitude. The operating temperature at large heat

722 load is higher than that at small heat load under acceleration conditions. Moreover, the effect of
723 the acceleration force on the loop temperature becomes weak when the acceleration magnitude
724 exceeds 5 g at 80 W. The operating temperatures are 32.2 °C, 26.7 °C, 28.4 °C, 27.4 °C and 27.0
725 °C at 3 g, 5 g, 7 g, 9 g and 11 g, respectively. When the heat load is 200 W, it is more than 7 g
726 that the effect of the acceleration force becomes weak. The operating temperatures are 45.7 °C,
727 40.6 °C, 36.0 °C, 33.3 °C, 33.1 °C and 34.1 °C at 0g, 3g, 5g, 7g, 9g and 11g, respectively.

728 As can be seen in Fig. 14(b), the thermal conductance shows an obvious increase with the
729 increase of the acceleration magnitude under configuration C. In accord with the operating
730 temperature change, thermal conductance at large heat load is also larger than that at small heat
731 load under acceleration conditions. When the acceleration magnitude is below 7 g at 200 W,
732 the range of the thermal conductance is from 8.5 W/K to 16.0 W/K. As the acceleration
733 magnitude is above 7 g, the thermal conductance ranges from 20.9 W/K to 22.9 W/K. The
734 DCCLHP operates at CCM when coupled with RTD 9 and RTD10 temperatures. However,
735 when the heat load is 80 W, the thermal conductance ranges from 10.3 W/K to 19.8 W/K under
736 the range of acceleration magnitude from 3 g to 11 g. it operates at VCM at 3 g whereas at
737 CCM under 5 g and 11 g conditions.

738 Based on above describes, the DCCLHP could start up under different acceleration
739 magnitude and direction conditions. The operating temperature is susceptible to the
740 acceleration magnitude at large heat load and shows a general trend of decrease with the
741 increase of the acceleration magnitude at small heat load. Under configuration B the loop
742 appeared temperature oscillations and operates at a quasi-steady state as the heat load is 250 W
743 and 300 W. The acceleration magnitude could impact on the amplitude and period of the
744 oscillation. Furthermore, it could change the operating mode of the loop.

745 **5. Conclusions**

746 Experimental studies were conducted to investigate the startup behavior and operating
747 characteristics of a DCCLHP with insufficient fluid inventory. The impact of the various
748 control parameters such as heat load, acceleration magnitude and acceleration direction was
749 analyzed in a systematic manner. Major findings based on the experimental results were as
750 follows:

751 (1) The DCCLHP can start up at the small heat load of 25 W under acceleration conditions.

752 It started up within a very short time at large heat load. Even at a fixed heat load, the DCCLHP
753 can have a different startup behavior as it was subjected to different direction acceleration force,
754 owing to the different vapor-liquid distribution in the evaporator and CCs.

755 (2) In general, the operating temperature was higher in terrestrial gravity than that under
756 acceleration conditions. The impact of acceleration direction and magnitude on the operating
757 temperature was significant at small heat load (≤ 150 W). But it was weak at large heat load.
758 The acceleration force effect can change the heat load range of VCM or CCM.

759 (3) As the acceleration force contributed to the liquid returning back to the CCs, like under
760 configuration C, the acceleration force effect was similar to the gravity-assisted effect. At small
761 heat load, the entire loop temperatures had an approximate 1.0 °C difference and the operating
762 temperature was small.

763 (4) A number of temperature oscillation, reverse flow and evaporation in the evaporator core
764 phenomena were observed under acceleration conditions. Especially under configuration B, it
765 was at 250 W and 300 W that periodic temperature oscillations occurred on almost the whole
766 loop for different acceleration magnitudes.

767 **Acknowledgement**

768 The authors acknowledge the financial supports from the Fundamental Research Funds
769 for the Central Universities of China (YWF-14-HKXY-019) and the National Natural Science
770 Foundation of China (No.51406009) as well as research funding from University of
771 Hertfordshire.

772

773 **References**

- 774 [1] X. Chen, H. Ye, X. Fan, et al., A review of small heat pipes for electronics, *Applied*
775 *Thermal Engineering* 96 (2016) 1-17.
- 776 [2] A. Faghri, Review and advances in heat pipe science and technology, *Journal of Heat*
777 *Transfer* 134 (12) (2012) 123001-123019.
- 778 [3] Y. F. Maydanik, Loop heat pipes, *Applied Thermal Engineering* 25 (2005) 635-657.
- 779 [4] A. Ambirajan, A. A. Adoni, J. S. Vaidya, *et al.*, Loop heat pipes: A review of fundamentals,
780 operation, and design, *Heat Transfer Engineering* 33 (4-5) (2012) 387-405
- 781 [5] B. Siedel, V. Sartre, F. Lefèvre, Literature review: Steady-state modelling of loop heat pipes,

782 Applied Thermal Engineering 75 (2015) 709-723.

783 [6] J. Ku, Operating characteristics of loop heat pipes, SAE Paper No.1999-01-2007, 1999.

784 [7] T. Tharayil, L. G. Asirvatham, V. Ravindran, et al., Thermal performance of miniature loop
785 heat pipe with grapheme-water nanofluid, International Journal of Heat and Mass Transfer,
786 93 (2016): 957-968.

787 [8] M. A. Chernysheva and Yu. F. Maydanik, Effect of liquid filtration in a wick on thermal
788 processes in a flat disk-shaped evaporator of a loop heat pipe, International Journal of Heat
789 and Mass Transfer, 106 (2017): 222-231.

790 [9] J. He, J. Y. Miao, L. Z. Bai, et al., Effect of non-condensable gas on the startup of a loop
791 heat pipe, Applied Thermal Engineering, 111(25) (2017) 1507-1516.

792 [10] V. S. Jasvanth, A. A. Adoni, V. Jaikumar, et al., Design and testing of an ammonia loop
793 heat pipe, Applied Thermal Engineering, 111(25) (2017) 1655-1663.

794 [11] H. X. Zhang, G. P. Lin, T. Ding, et al., Investigation on startup behaviors of a loop heat
795 pipe, Journal of Thermophysics and Heat Transfer, 19 (4) (2005) 509-518.

796 [12] Y. Chen, M. Groll, R. Mertz, et al., Steady-state and transient performance of a miniature
797 loop heat pipe, International Journal of Thermal Sciences, 45 (11) (2006) 1084-1090.

798 [13] C. Gerhart and D. F. Gluck, Summary of operating characteristics of a dual compensation
799 chamber loop heat pipe in gravity, In: Proceeding of the 11th International Heat Pipe
800 Conference, Tokyo, Japan, 1999, pp. 67-68.

801 [14] D. F. Gluck, C. Gerhart, S. Stanley, Characterization of a high capacity, dual
802 compensation chamber loop heat pipe, American Institute of Physics Conference
803 Proceedings, 458(1) (1999) 943-948.

804 [15] D. A. Wolf and W. B. Bienert, Investigation of temperature control characteristics of loop
805 heat pipe, SAE Paper No.941576, 1994.

806 [16] J. B. Long and J. M. Ochterbeck, Transient/cyclic heat loads for dual compensation
807 chamber loop heat pipes, Proceedings of XIIHPC, Japan Association for Heat Pipes, Tokyo,
808 Japan, 1999, pp. 305-310.

809 [17] G. P. Lin, H. X. Zhang, X. G. Shao, et al., Development and test results of a dual
810 compensation chamber loop heat pipe, Journal of Thermophysics and Heat Transfer, 20 (4)
811 (2006) 825-834.

- 812 [18] L.Z. Bai, G. P. Lin, D. S. Wen, et al., Experimental investigation of startup behaviors of a
813 dual compensation chamber loop heat pipe with insufficient fluid inventory, *Applied*
814 *Thermal Engineering*, 29 (8) (2009) 1447-1456.
- 815 [19] G. P. Lin, N. Li, L. Z. Bai, et al, Experimental investigation of a dual compensation
816 chamber loop heat pipe, *International Journal of Heat and Mass Transfer*, 53(2010)
817 3231-3240.
- 818 [20] Y. Zhao, S. Chang, B. Yang, et al., Experimental study on the thermal performance of
819 loop heat pipe for the aircraft anti-icing system, *International Journal of Heat and Mass*
820 *Transfer*, 111 (2017) 795-803.
- 821 [21] J. Ku, L. Ottenstein, T. Kaya, et al., Testing of a loop heat pipe subjected to variable
822 accelerating forces, part 1: start-up, SAE Paper No. 2000-01-2488, 2000.
- 823 [22] J. Ku, L. Ottenstein, T. Kaya, et al., Testing of a loop heat pipe subjected to variable
824 accelerating forces, part2: temperature stability, SAE Paper No. 2000-01-2489, 2000.
- 825 [23] A. J. Fleming, S. K. Thomas, K. L. Yerkes, et al., Titanium-water loop heat pipe operating
826 characteristics under standard and elevated acceleration fields, *Journal of Thermophysics*
827 *and Heat Transfer*, 24 (1) (2010) 184-198.
- 828 [24] K. L. Yerkes, J. D. Scofield, D. L. Courson, et al., Steady-periodic acceleration effects on
829 the performance of a loop heat pipe, *Journal of Thermophysics and Heat Transfer*, 28 (3)
830 (2014) 440-454.
- 831 [25] K. L. Yerkes, J. D. Scofield, D. L. Courson, Performance of a loop heat pipe subjected to
832 a phase-coupled heat input to an acceleration field, In: the 46th AIAA Thermophysics
833 Conference, AIAA paper No. 2016-4145, 2016.
- 834 [26] Y. Q. Xie, J. Zhang, L. Y. Xie, et al., Experimental investigation on the operating
835 characteristics of a dual compensation chamber loop heat pipe subjected to acceleration
836 field, *Applied Thermal Engineering*, 81 (2015) 297-312.
- 837 [27] J. Z. Yu, Principle and design of heat exchanger, first edition, Beihang University
838 Publication, Beijing, 2006, p. 239.
- 839 [28]Moffat R J, Describing the uncertainties in experimental results, *Experimental thermal and*
840 *fluid science*, 1988, 1(1): 3-17.

841 Fig. 1. The schematic diagram of the experimental system.

842 Fig. 2. A photo of the centrifuge and the test section enclosure.

843 Fig. 3. A picture of the experimental DCCLHP and detailed construction of evaporator and
844 CCs. (a) the DCCLHP (b) detailed construction of evaporator and CCs

845 Fig. 4. Schematic of the DCCLHP and RTDs locations.

846 Fig. 5. Three different directions of the acceleration. (a) Configuration A (b) Configuration B
847 (c) Configuration C

848 Fig. 6. The loop temperature profiles at 5g and 25 W under configuration A, B and C. (a)
849 Configuration A (b) Configuration B (c) Configuration C.

850 Fig. 7. Vapor-liquid distribution in the loop under configuration A, B and C. (a) Configuration
851 A (b) Configuration B (c) Configuration C.

852 Fig. 8. The loop temperature profiles at 250 W and 5 g under configuration A, B and C. (a)
853 Configuration A (b) Configuration B (c) Configuration C.

854 Fig. 9. The operating temperature and thermal conductance at 5g under three configurations
855 and terrestrial gravity. (a) Temperature (b) Thermal conductance.

856 Fig. 10. The loop temperature profiles at 80 W under terrestrial gravity and under
857 configuration A at 5 g. (a) Terrestrial gravity (b) Configuration A at 5 g.

858 Fig. 11. The loop temperature evolutions at 300 W and 3 g, 5 g, 7 g and 9 g under
859 configuration B.

860 Fig. 12. The operating temperature and thermal conductance at 150 W, 250 W and 300 W
861 under acceleration conditions for configuration B. (a) Temperature (b) Thermal
862 conductance.

863 Fig. 13. The loop temperature evolutions at 80 W and 3 g, 5 g, 7 g, 9 g and 11 g under
864 configuration C.

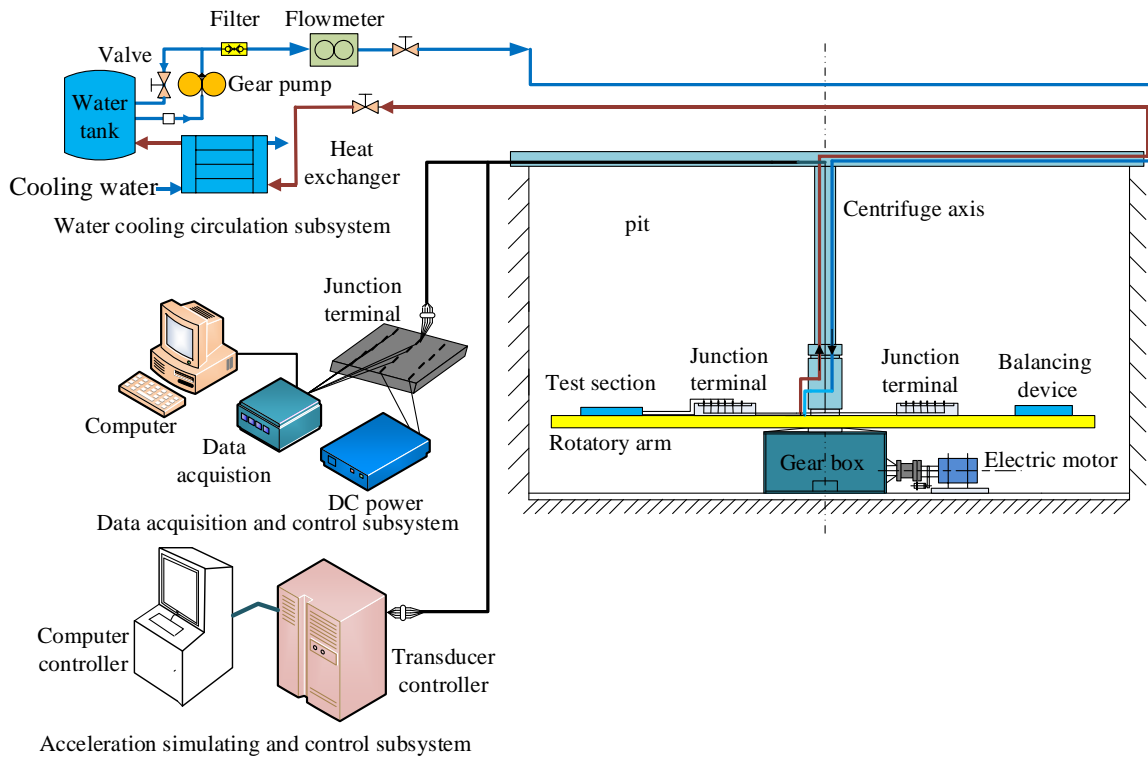
865 Fig. 14. The operating temperature and thermal conductance at 80 W and 200 W under
866 acceleration conditions for configuration C. (a) Temperature (b) Thermal conductance.

867 Table 1. Major design parameters of the experimental DCCLHP

868

869

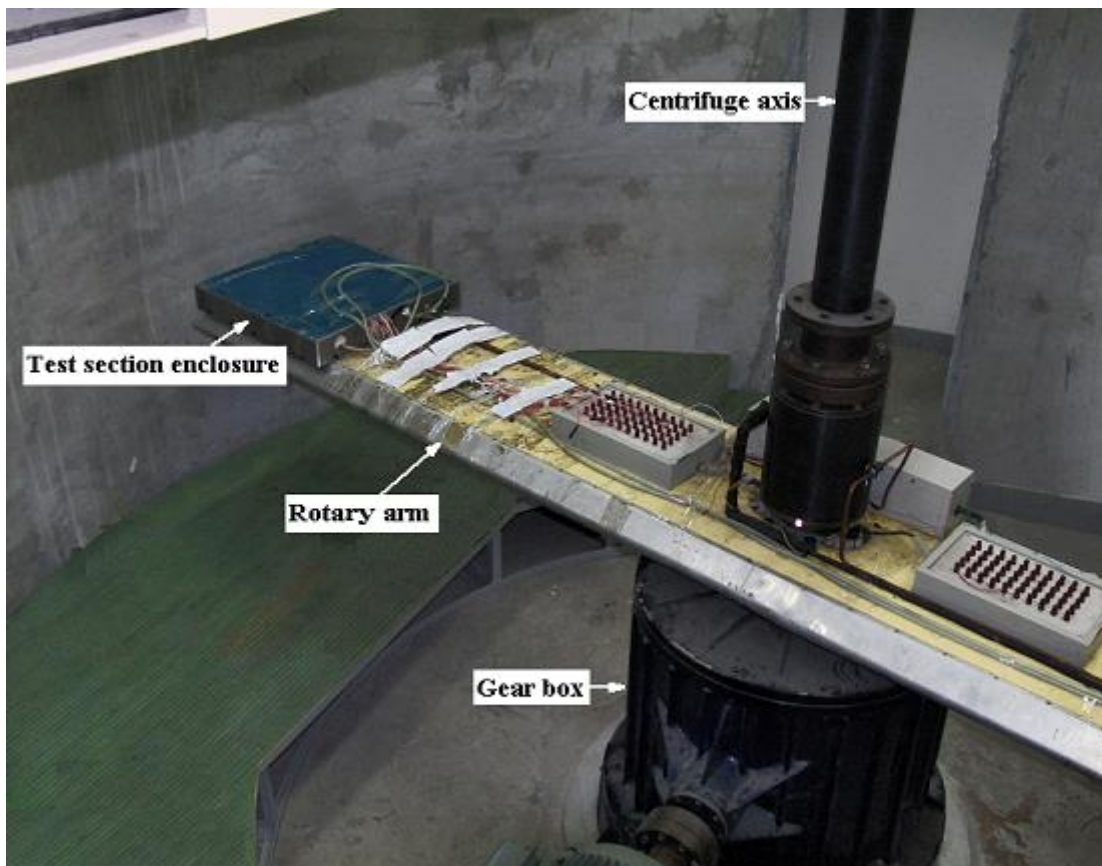
870



871

872

Fig. 1. The schematic diagram of the experimental system.



873

874

875

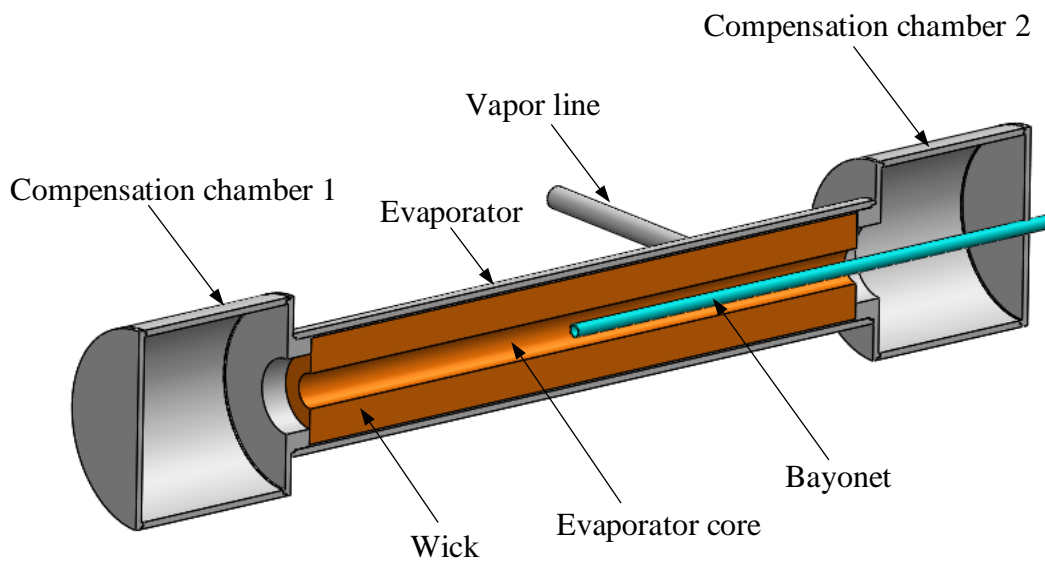
Fig.2. A photo of the centrifuge and the test section enclosure.



876

877

(a)



878

879

(b)

Fig.3. A picture of the experimental DCCLHP and detailed construction of evaporator and CCs. (a) the DCCLHP (b) detailed construction of evaporator and CCs.

881

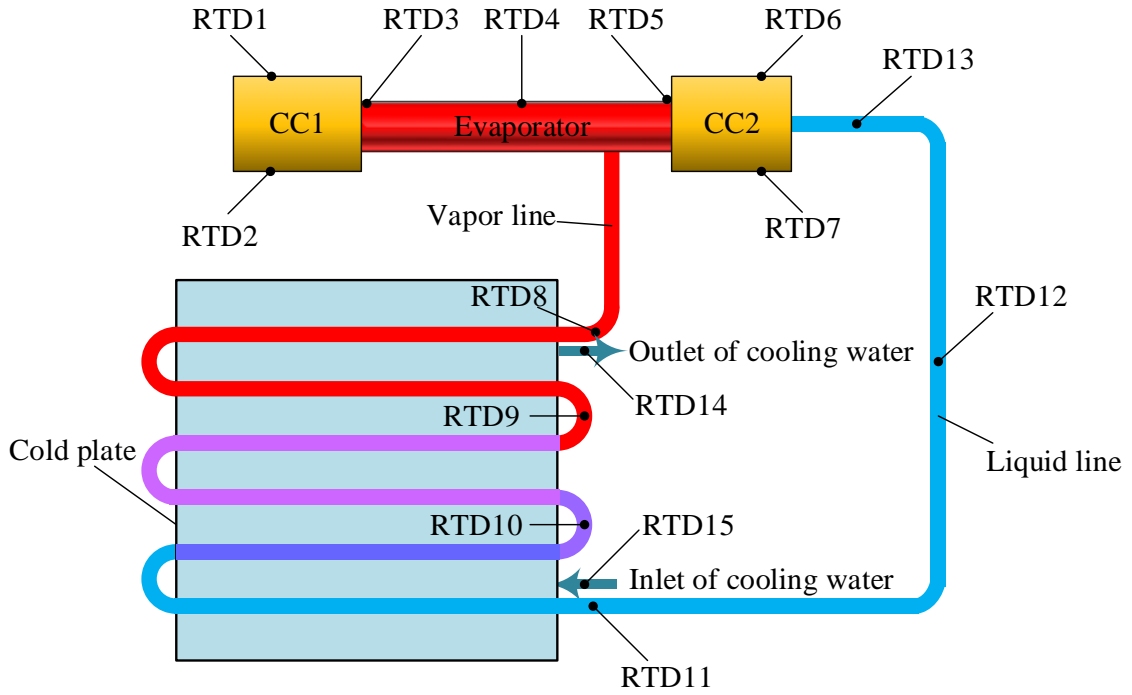
882

883

884

885

886

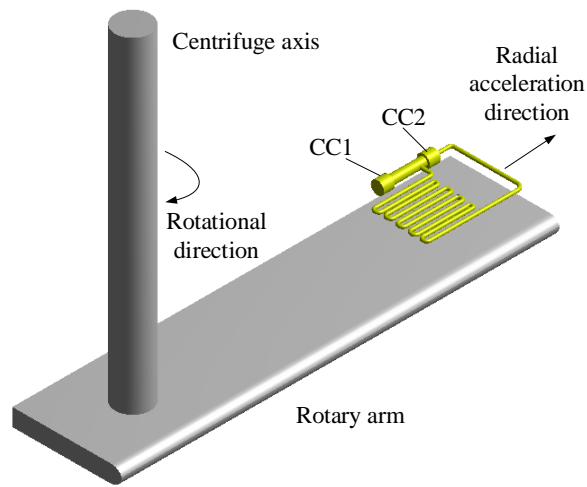


887

888

Fig.4. Schematic of the DCCLHP and RTDs locations.

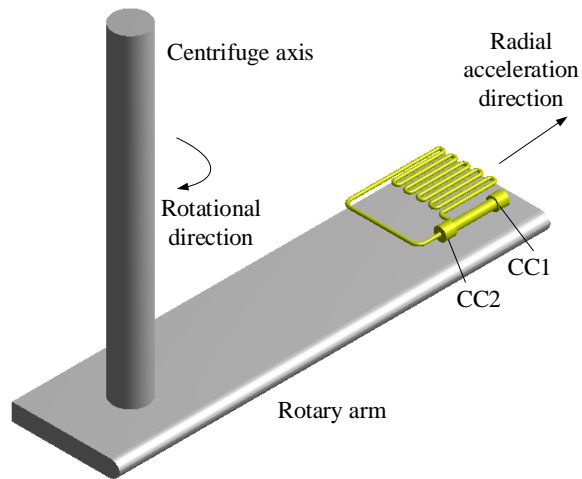
889



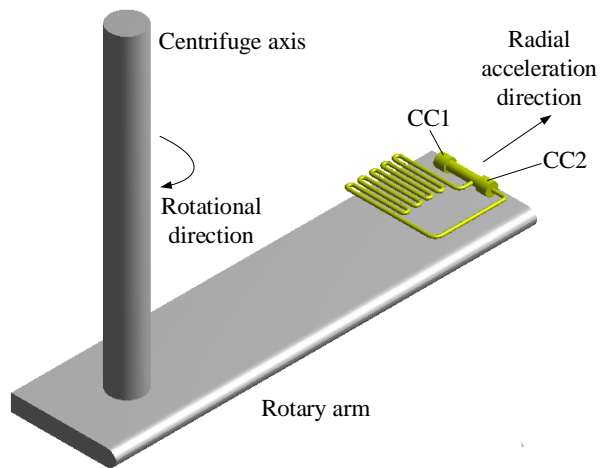
890

891

(a)

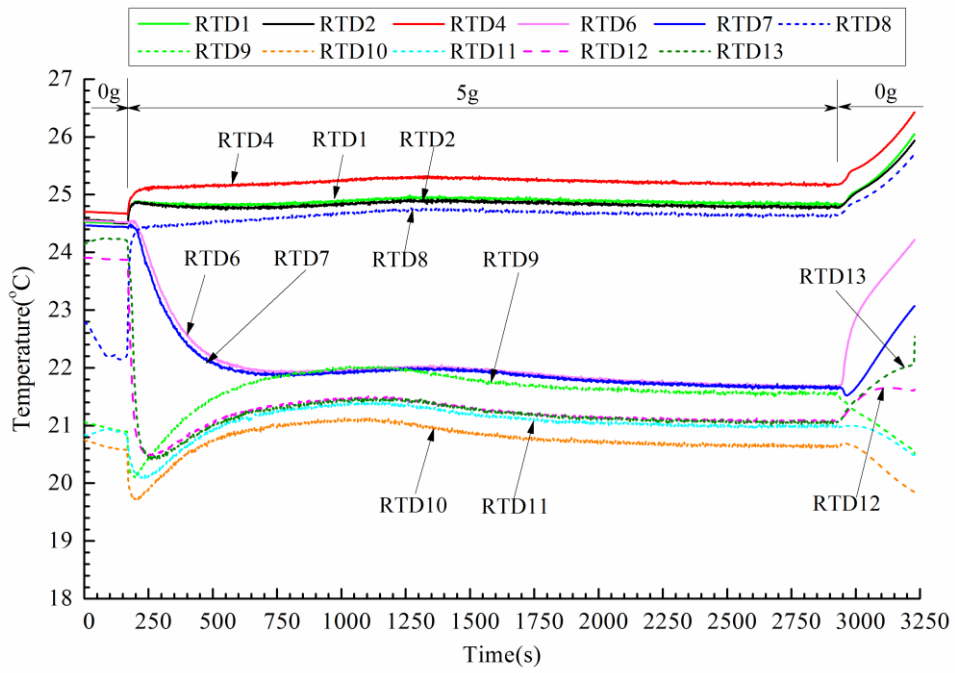


(b)



(c)

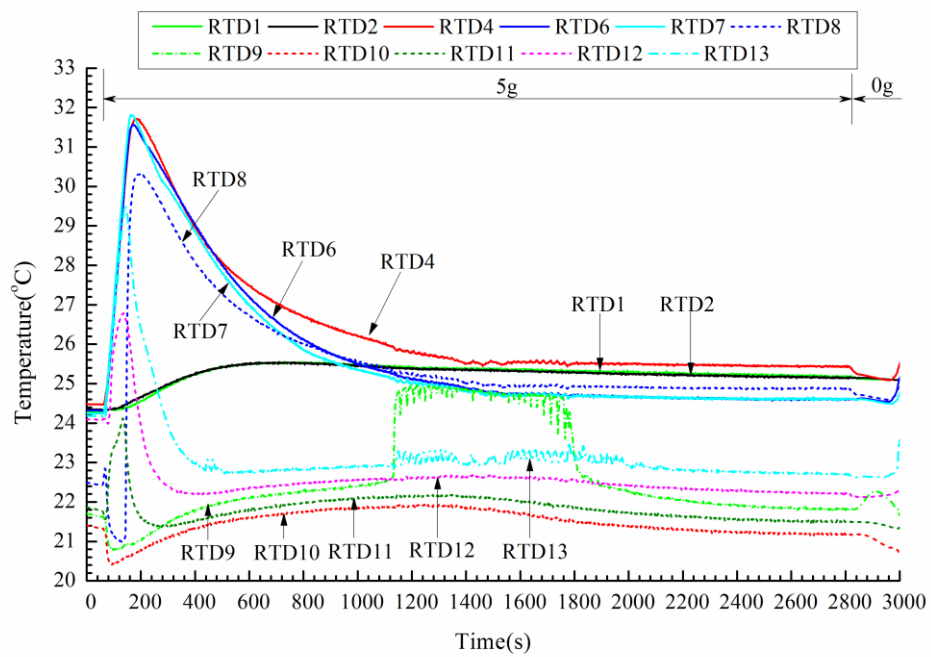
Fig.5. Three different directions of the acceleration. (a) Configuration A (b) Configuration B (c) Configuration C



899

900

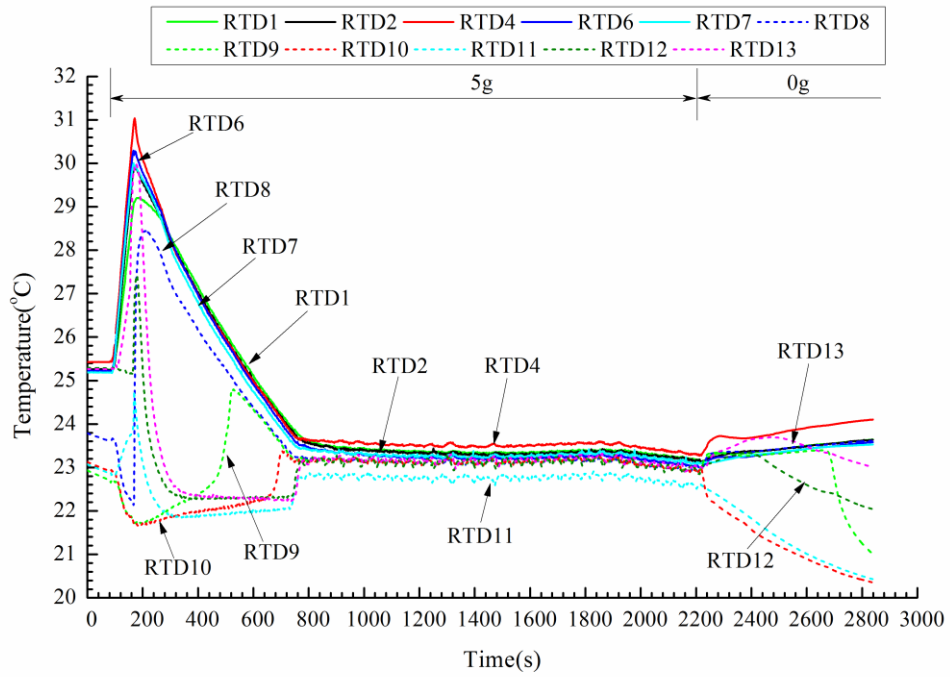
(a)



901

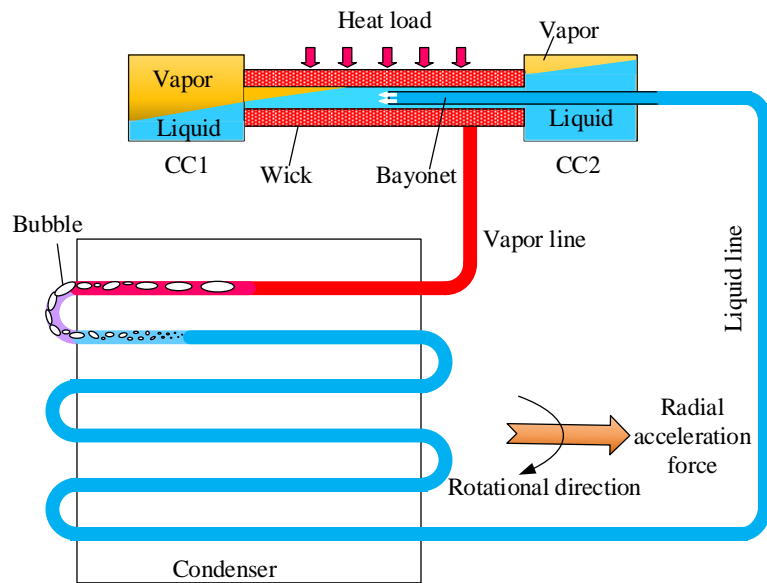
902

(b)

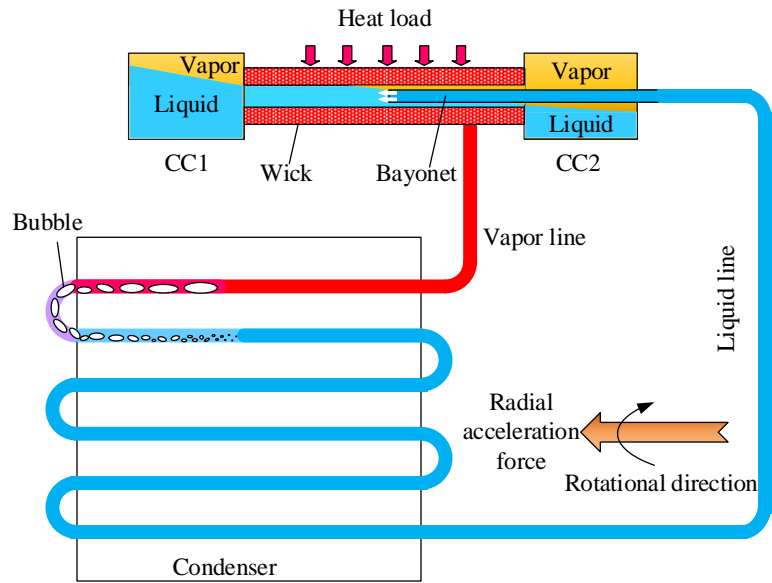


(c)

Fig. 6. The loop temperature profiles at 5 g and 25 W under three configurations. (a) Configuration A (b) Configuration B (c) Configuration C.



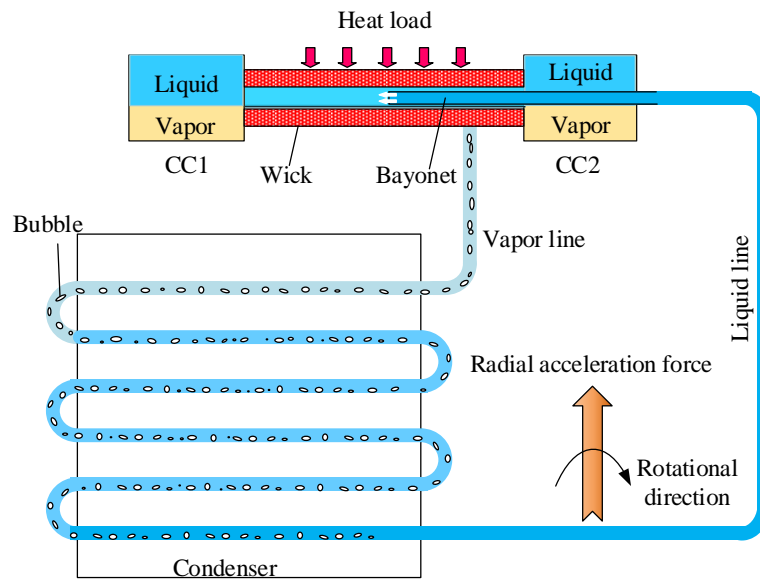
(a)



910

911

(b)



912

913

(c)

Fig. 7. Vapor-liquid distribution in the loop under configuration A, B and C. (a)

Configuration A (b) Configuration B (c) Configuration C.

915

916

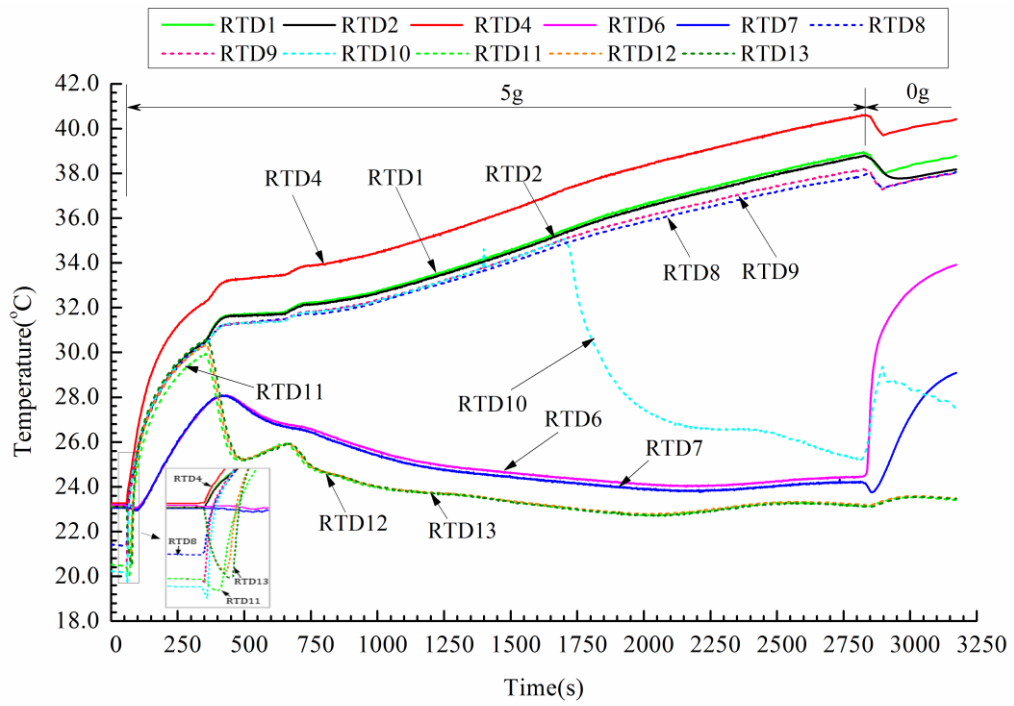
917

918

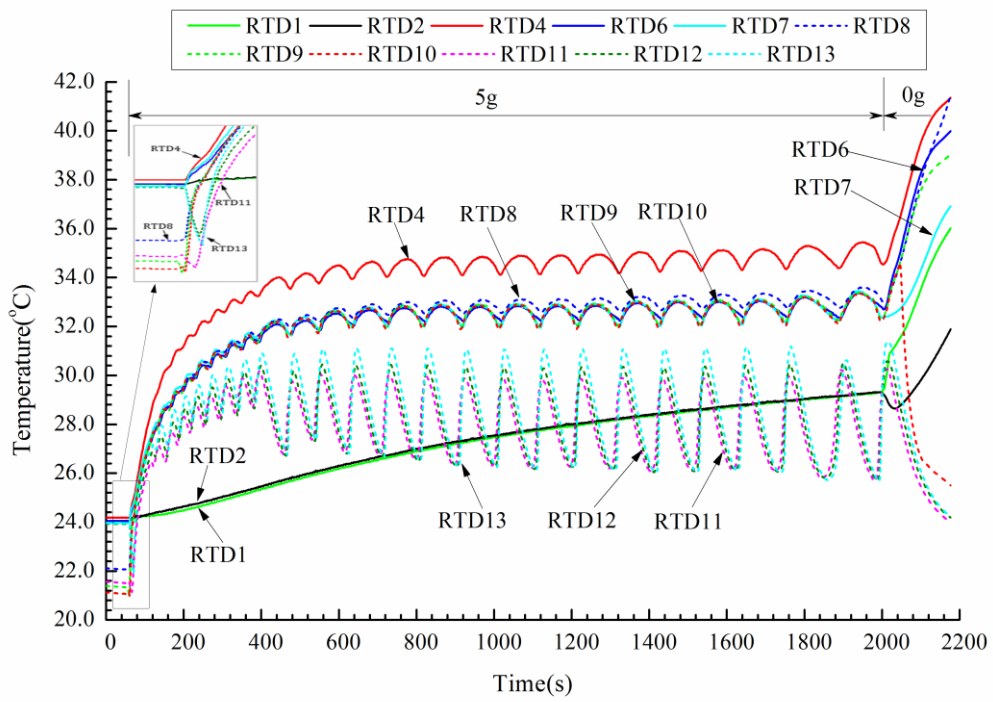
919

920

921



(a)



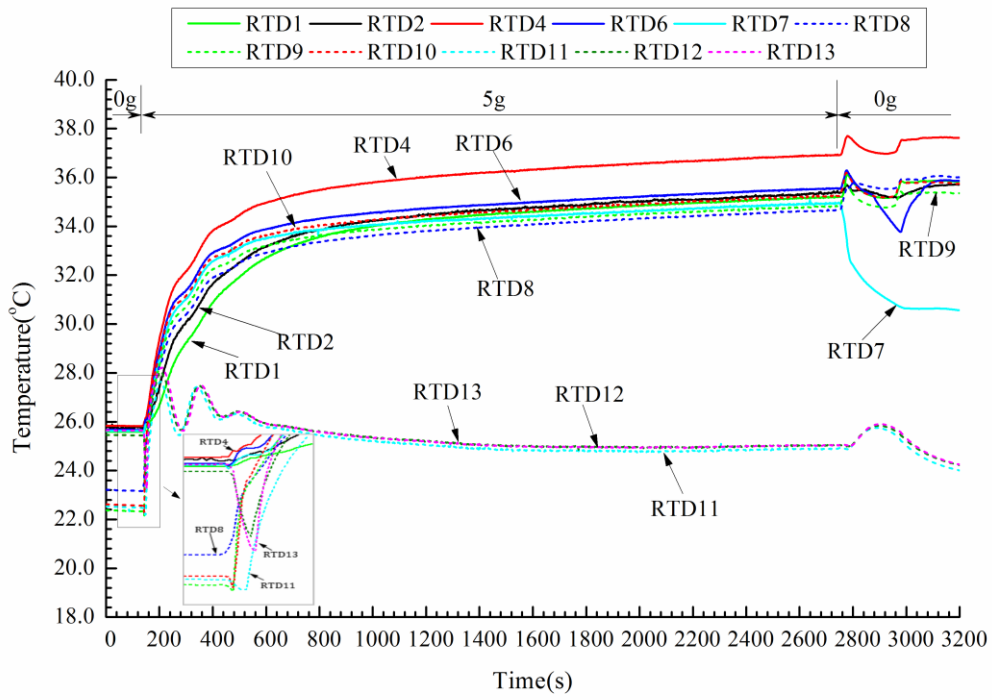
(b)

922

923

924

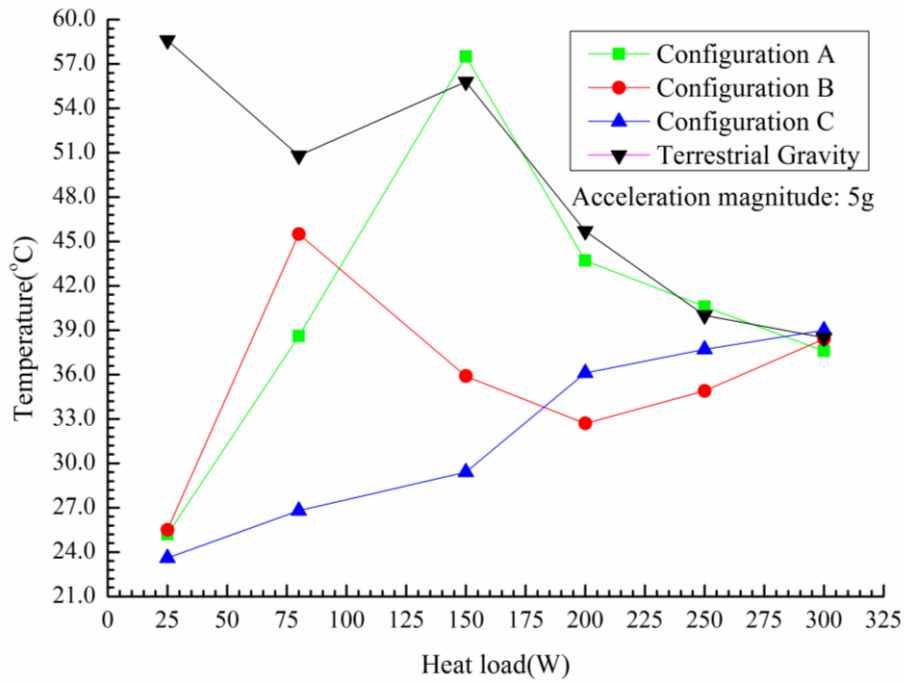
925



(c)

Fig. 8 The loop temperature profiles at 250 W and 5 g under configuration A, B and C. (a)

Configuration A (b) Configuration B (c) Configuration C.



(a)

926

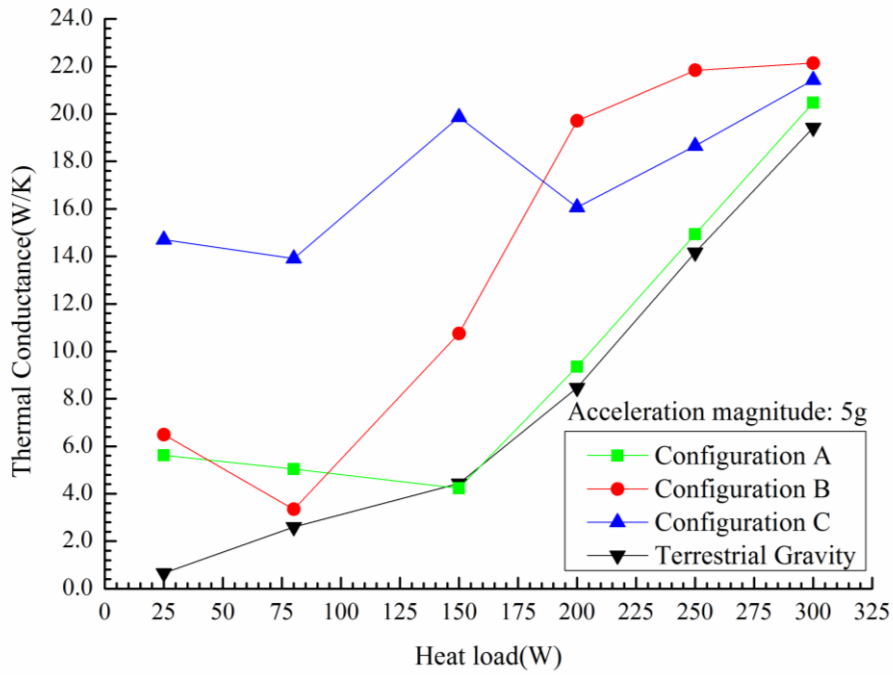
927

928

929

930

931



932

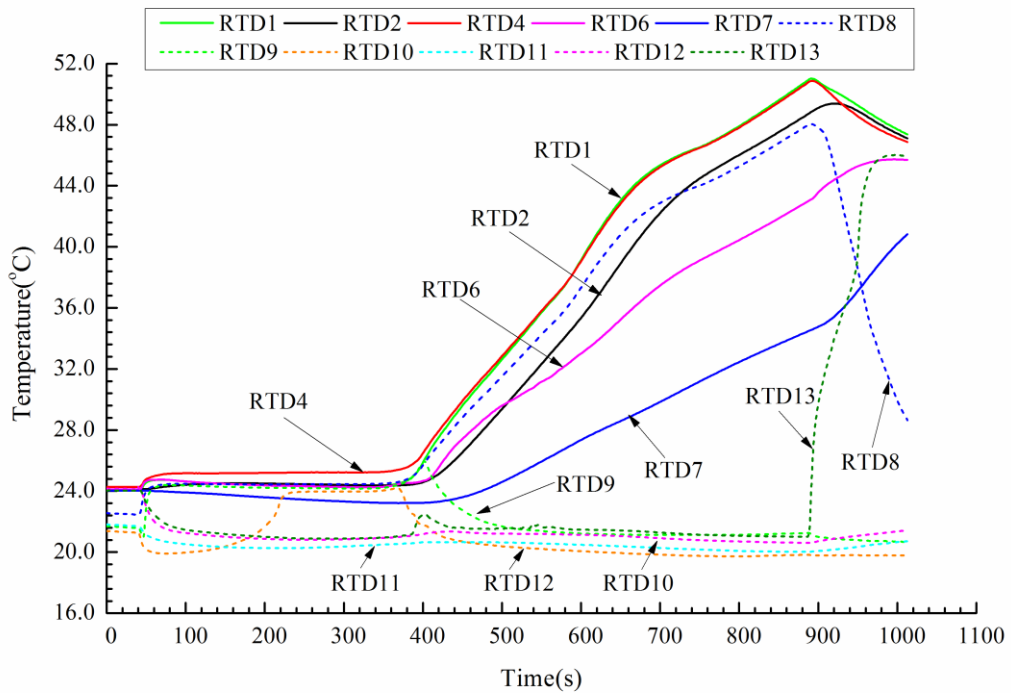
933

(b)

934 Fig.9. The operating temperature and thermal conductance at 5 g under three configurations

935

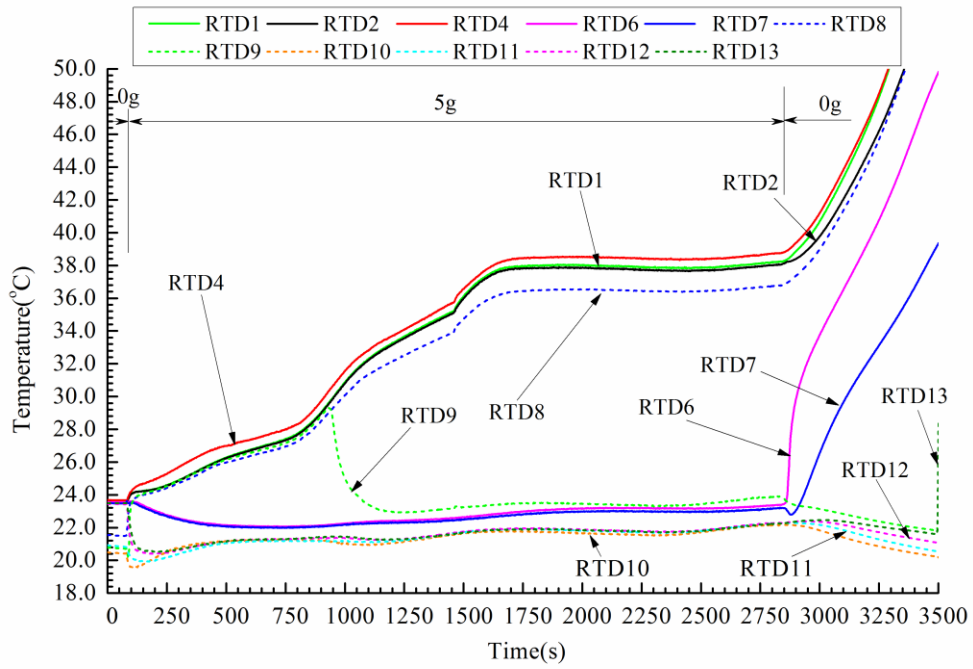
and terrestrial gravity. (a) Temperature (b) Thermal conductance.



936

937

(a)



(b)

Fig.10 The loop temperature profiles at 80 W under terrestrial gravity and under configuration

A at 5 g. (a) Terrestrial gravity (b) Configuration A at 5 g.

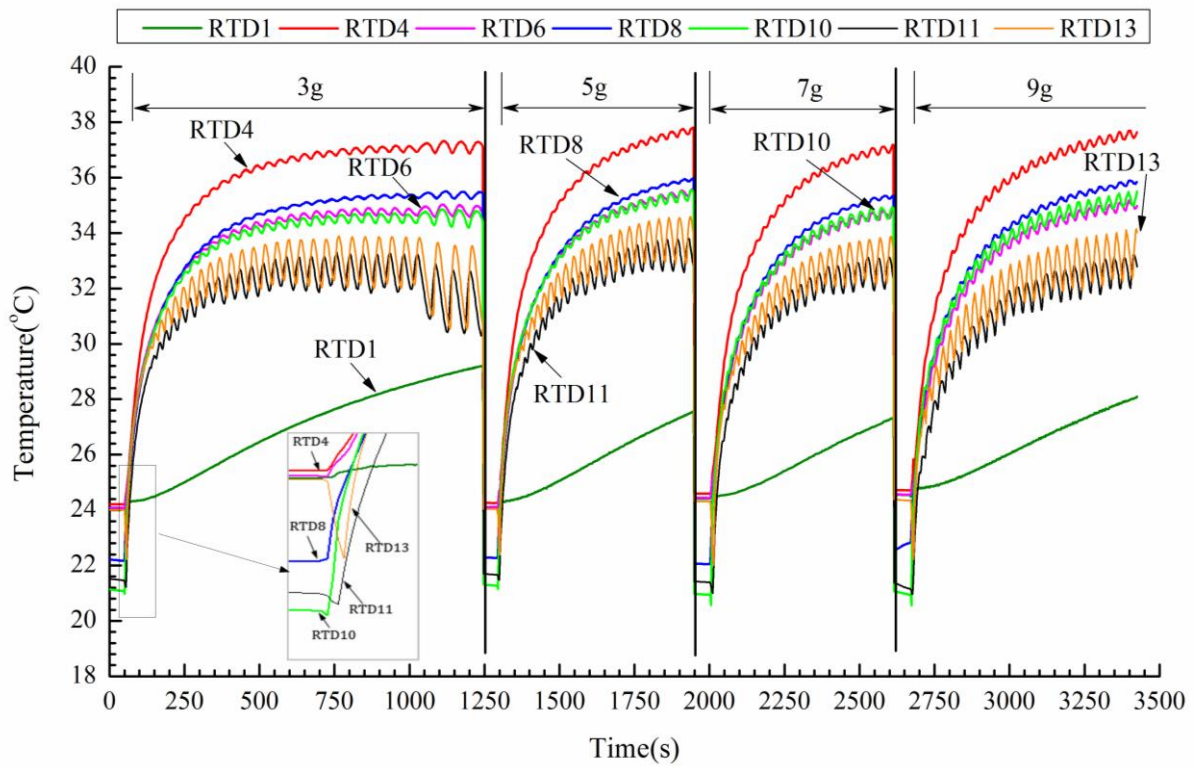
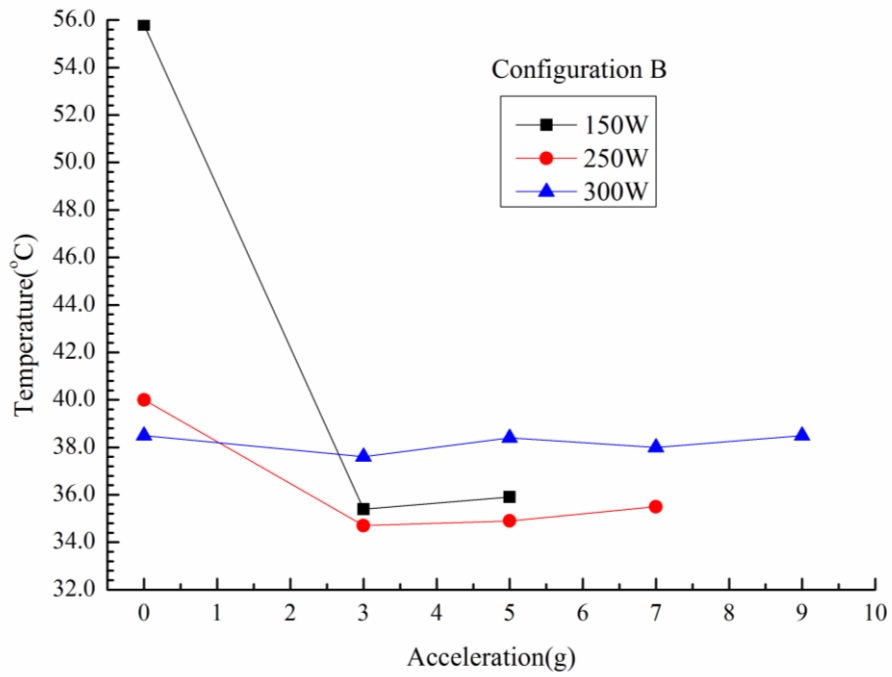


Fig.11. The loop temperature evolutions with different acceleration magnitude at 300 W

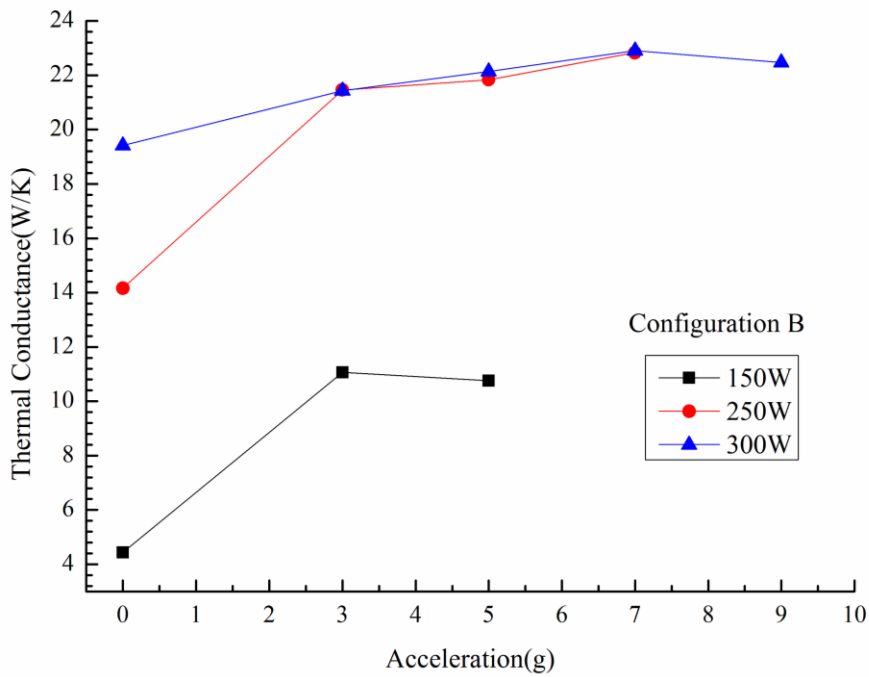
for configuration B.



945

946

(a)



947

948

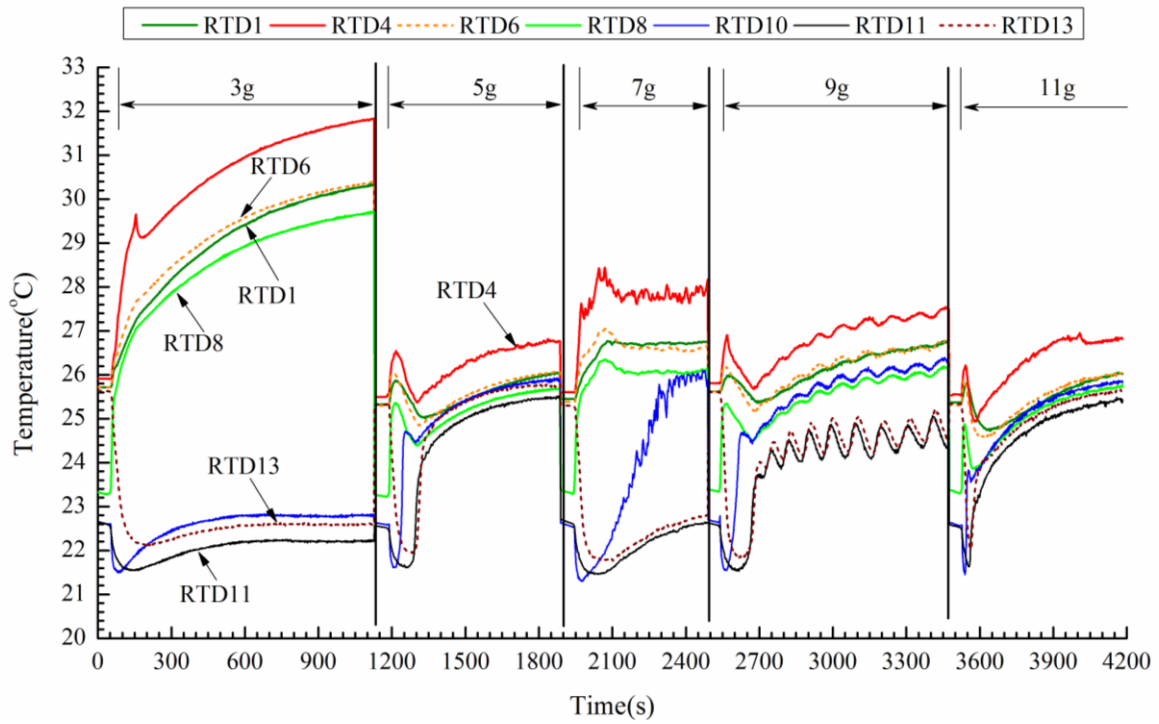
(b)

949 Fig.12. The operating temperature and thermal conductance at 150 W, 250 W and 300 W
 950 under acceleration conditions for configuration B. (a) Temperature (b) Thermal conductance.

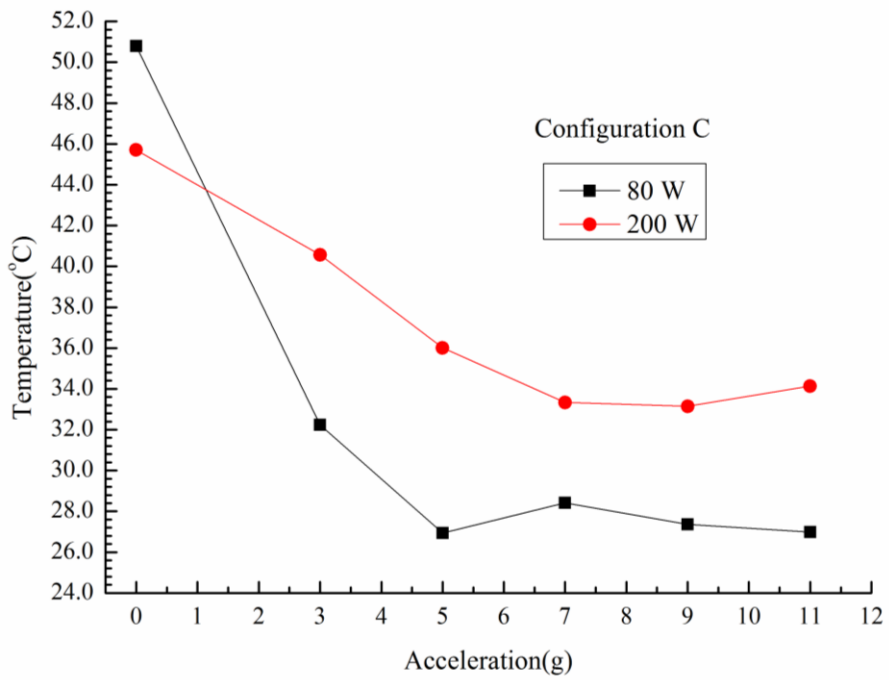
951

952

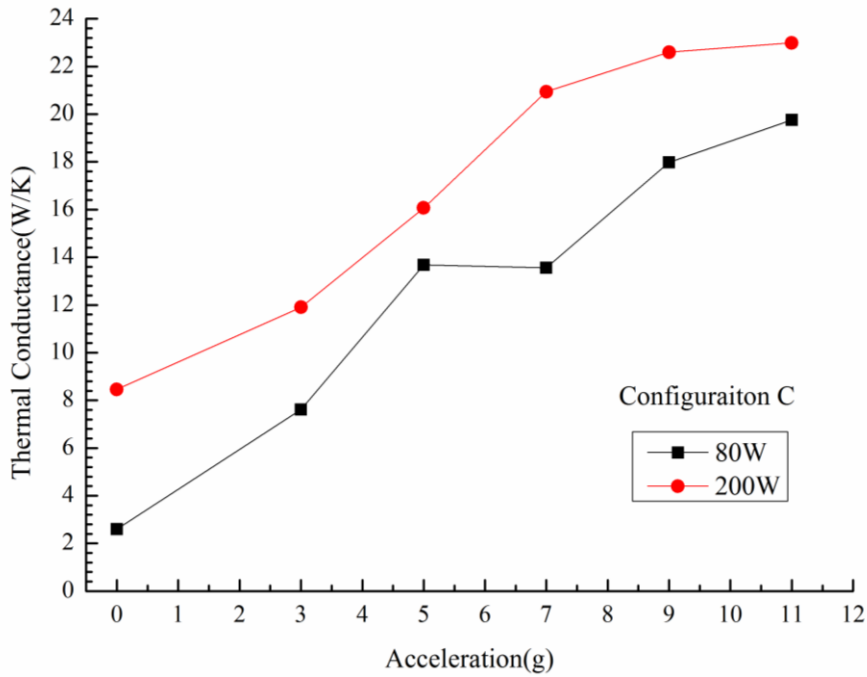
953



954
 955 Fig.13. The loop temperature evolutions with different acceleration magnitude at 80 W for
 956 configuration C.



957
 958 (a)



(b)

Fig.14. The operating temperature and thermal conductance at 80 W and 200 W under acceleration conditions for configuration C. (a) Temperature (b) Thermal conductance.

Evaporator	O.d./i.d.×length of casing	20 mm/18 mm×209 mm
	Material	Stainless steel
(primary) Wick	Pore radius	1.5 μm
	Porosity	$>5 \times 10^{-14} \text{ m}^2$
	O.d./i.d.×length	18 mm/6 mm×190 mm
	Material	Nickel
Vapor line	O.d./i.d.×length	3 mm/2.6 mm×225 mm
	Material	Stainless steel
Liquid line	O.d./i.d.×length	3 mm/2.6 mm×650 mm
	Material	Stainless steel
Condenser line	O.d./i.d.×length	3 mm/2.6 mm×2200 mm
	Material	Stainless steel
Compensation chamber	O.d./i.d.×length	27 mm/25 mm×64 mm
	Material	Stainless steel
	Number	2
Working fluid	Ammonia	

Table 1 Major design parameters of the experimental DCCLHP